Mineralogy and Petrology (2019) 113:77–97
https://doi.org/10.1007/s00710-018-0636-1

ORIGINAL PAPER

Petrogenesis of early cretaceous andesite dykes in the Sulu orogenic belt, eastern China

Songjie Wang[1] · Xuping Li[1] · Hans-Peter Schertl[1,2] · Qingda Feng[1]

Received: 26 January 2018 / Accepted: 12 September 2018 / Published online: 28 September 2018
© Springer-Verlag GmbH Austria, part of Springer Nature 2018

Abstract

This study presents data of in-situ mineral major and trace element chemistry, whole-rock major and trace element and Sr–Nd isotope geochemistry, as well as zircon U–Pb dating and Lu–Hf isotope studies of andesite dykes from the Sulu orogenic belt of eastern China to evaluate their petrogenesis and thus to provide insights into crust–mantle interactions in a tectonic terrane that underwent continental subduction and was then overprinted by oceanic subduction. The andesites mainly comprise plagioclase, hornblende, clinopyroxene and magnetite as phenocrysts that are embedded in a groundmass of fine-grained quartz and K-feldspar, with minor amounts of biotite, magnetite, titanite, apatite and zircon. They possess intermediate concentrations of SiO_2 (54.97–62.24 wt.%), $Na_2O + K_2O$ (6.35–7.24 wt.%) and MgO (3.37–7.12 wt.%) with high Mg# values [Mg# = 100 × Mg/(Mg + Fe^{2+}) molar] of 54–64, and are characterized by arc-like trace element patterns that are enriched in light rare earth elements (LREE) and large ion lithophile elements (LILE) but depleted in high field strength elements (HFSE). The hornblende and clinopyroxene phenocrysts exhibit enrichment in Th and U but an obvious depletion of HFSE. The andesites have high initial $^{87}Sr/^{86}Sr$ ratios of 0.7073–0.7086 and negative $\varepsilon_{Nd}(t)$ values of −15.7 to −14.4 for whole-rock, and newly crystallized magmatic zircons show negative $\varepsilon_{Hf}(t)$ values of −27.0 to −17.6. U–Pb dating on syn-magmatic zircons yields consistent ages of 124 ± 2 to 116 ± 1 Ma, indicating eruption of the andesitic lavas during the Early Cretaceous. Inherited zircons are present and yield Neoproterozoic, Paleoproterozoic and Archean U–Pb ages. Taking into account all these geochemical and geochronological data, and the compositional features of contemporaneously formed mafic–andesitic igneous rocks from the Sulu belt and the adjacent continental crust of the North China Craton, we propose that the andesites crystallized from primary andesitic magmas derived from partial melting of enriched metasomatites in the subcontinental lithospheric mantle. The enriched metasomatites are inferred to be formed by a two-step process: firstly by crust–mantle interactions during the Triassic collisional orogeny and secondly by a subsequent modification by fluids/melts that mainly derive from seafloor sediments during subduction of the paleo-Pacific plate in eastern Asia. Slab rollback of the subducted paleo-Pacific slab and concomitant asthenosphere upwelling are an appropriate geodynamic mechanism for the generation of extensive arc-like magmatism during the Early Cretaceous in the Sulu belt.

Keywords Continental subdution · Paleo-Pacific plate subduction · Andesitic magmatism · Sulu orogenic belt · Source mixing

Editorial handling: S. W. Faryad

Electronic supplementary material The online version of this article (https://doi.org/10.1007/s00710-018-0636-1) contains supplementary material, which is available to authorized users.

✉ Songjie Wang
cugsongjie@foxmail.com

[1] College of Earth Science and Engineering, Shandong University of Science and Technology, Qingdao 266590, China

[2] Institute of Geology, Mineralogy and Geophysics, Ruhr-University Bochum, 44780 Bochum, Germany

Introduction

Andesitic arc magmatism at active continental margins is one of the most pronounced manifestations of crust–mantle interactions in an oceanic subduction channel (e.g., Hildreth and Moorbath 1988; Peacock 1993; Stern 2002; Eiler 2003; Spandler and Pirard 2013). A wealth of studies have revealed that the andesitic rocks with typical arc-like geochemical signatures are produced by melting of the overlying mantle wedge that was metasomatized by fluid/melt released from the subducted oceanic crust (e.g., Hawkesworth et al. 1991). By contrast, due to limited fluid availability, syn-subduction

arc magmatism is absent during continental subduction (e.g., Rumble et al. 2003). However, the widespread occurrence of post-orogenic magmatic rocks in continental collisional orogens indicates that subcontinental lithospheric mantle (SCLM) on the top of deeply subducted continental crust could also be modified at the slab–mantle interface (e.g., Schaltegger 1997; Altherr et al. 2000; Gerdes et al. 2000; Zheng 2012). Therefore, these rocks preserve key information for the fertilization of the SCLM wedge and thus provide an important approach to decipher when and how did the crust–mantle interactions occur in the context of plate subduction. In the last three decades, although numerous studies have been performed on the generation and exhumation of ultrahigh-pressure (UHP) metamorphic rocks and attendant fluid/melt flow during continental collision (e.g., Chopin 2003; Hermann and Rubatto 2014; Cao et al. 2017), relatively less attention has been paid to encode the petrogenesis of post-orogenic magmatic rocks. What factors caused the extensive magmatism within collisional orogenic belts and the adjacent continental margins? How did the diverse magmatic rocks with mafic to felsic compositions form? What geodynamic mechanisms provided the required heat? Insights to these questions require detailed petrological, geochemical and geochronological constraints on targeted samples from representative regions.

The Dabie–Sulu orogen in central–eastern China has long been recognized as one of the largest UHP metamorphic belts in the world (Fig. 1; Hacker et al. 2000). This orogen underwent two vital stages of plate convergence during the Mesozoic, including the northward direct collision and movement of the Yangtze Craton beneath the North China Craton since the Late Triassic (e.g., Hacker et al. 2006), and the westward subduction of the paleo-Pacific plate in eastern Asia during the Jurassic to Cretaceous (Maruyama et al. 1997; Zhao and Ohtani 2009; Kusky et al. 2014), both contributing to significant modification and reworking of the ancient SCLM beneath the North China Craton. As a result, Late Mesozoic igneous rocks are widely exposed throughout the Dabie–Sulu orogen and the adjacent continental crust of the North China Craton (e.g., Jahn et al. 1999; Guo et al. 2004; Zhao et al. 2013; Zheng et al. 2018), gaining insight into the process of crustal recycling in mantle depths in a complex subduction-zone environment, and contributing to evaluate the geodynamic influences of the paleo-Pacific subduction in eastern Asian continent. Previous studies mainly concentrated on mafic igneous rocks and coeval granitoids in this region (e.g., Zheng et al. 2018), whereas the minor portion of post-orogenic andesitic rock suites has attracted less attention. The petrogenesis of andesite is controlled by multiple factors, such as chemical compositions of the melting source, the degree of flux/melt–peridotite reaction, source or magma mixing, fractional crystallization and crustal contamination (Gómez-Tuena et al. 2014). Until now, it is still controversial whether andesites that occur at both oceanic and continental subduction zones were crystallized from primary andesitic magmas or from various types of differentiated basaltic magmas (e.g., Kuno 1968; Hildreth and Moorbath 1988; Annen et al. 2005; Reubi and Blundy 2009; Straub et al. 2011; Meng et al. 2018). It has to be considered that they may also have experienced crustal contamination (e.g., Gill 1981; Gencalioglu Kuscu and Geneli 2010).

Here we present the results of petrography, mineral and whole-rock major and trace element and Sr–Nd isotope geochemistry, zircon U–Pb dating and in-situ Lu–Hf isotope studies of andesite dykes in the central Sulu belt to provide a comprehensive understanding of their petrogenesis in the context of continental/oceanic subduction. Our study is of help to illustrate on crust–mantle interactions and reworking of ancient SCLM in other collisional orogens worldwide, such as the Himalaya–Tibet in South Asia, the North Qaidam and South Altyn in China and the Western Gneiss Region in Norway.

Geological setting and sampling

The Sulu belt in Shandong peninsula represents the eastern segment of the Dabie–Sulu orogen that was produced from the northward collision and subduction of the Yangtze Craton beneath the North China Craton during the Triassic (e.g., Hacker et al. 2000; Ernst et al. 2007; Ni et al. 2013, 2016; Wang et al. 2018). It is bounded by the Wulian–Yantai fault to the north and the Jiashan–Xiangshui fault to the south and was offset northward by ~500 km from the Dabie belt along the NNE-trending sinistral Tan-Lu fault during the Cretaceous (Fig. 1; Xu and Zhu 1994). Further north beyond the Wulian–Yantai fault the Jiaobei terrane is located which is predominated by Neoarchean tonalite–trondhjemite–granodiorite gneisses and Paleoproterozoic metasedimentary sequences, belonging to the easternmost part of the North China Craton (Tang et al. 2008). Based on integrated field, petrological and geochemical studies, the Sulu belt is subdivided into a southern HP and a northern UHP metamorphic zone (e.g., Li et al. 2014). The UHP zone is primarily composed of gneisses, with minor amounts of eclogite, garnet peridotite, quartzite and marble. Coesite was recognized in eclogite and as inclusions in zircon from both the eclogite and the country rocks such as gneiss and marble, indicating that all these units underwent a joint in-situ UHP metamorphism at mantle depths >90 km (e.g., Liu and Liou 2011). The protoliths of these UHP rocks were mostly produced in a continental rift setting during the Neoproterozoic, probably in relation to the breakup of the supercontinent Rodinia (e.g., Zheng et al. 2005).

Of special interest in recent years is the partial melting these UHP rocks experienced during the latest stage of

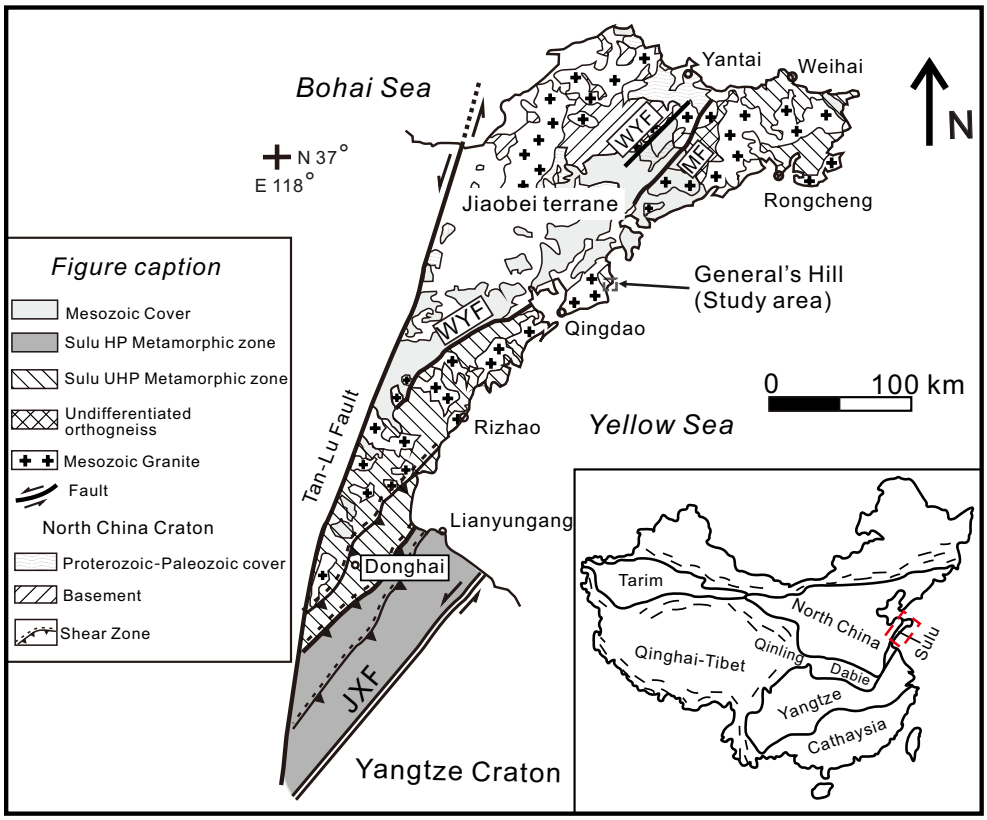

Fig. 1 Geological sketch map of the Sulu orogenic belt (after Yoshida et al. 2004); the insert shows the tectonic location of the Sulu belt in China; WYF: Wulian–Yantai Fault; JXF: Jiashan–Xiangshui Fault; the grey framed area at General's Hill was in part shown in Fig. 2 of Wang et al. (2017) and also in Fig. S1 of this study

subduction to subsequent exhumation (e.g., Wang et al. 2014; Xia et al. 2018). Abundant studies have shown that different types of UHP rocks, including gneiss, eclogite and kyanite quartzite, were partially melted mainly induced by the release of water from nominally anhydrous minerals and breakdown of hydrous minerals including phengite/zoisite, leaving micro-scale multiphase solid inclusions to macro-scale granitic dykes and plutons as products (e.g., Hermann and Rubatto 2014; Wang et al. 2016, 2017). According to integrated geochemical and geochronological studies on mantle-derived garnet peridotites and syn-exhumation magmatic rocks (*c.*212–201 Ma) of this region, some researchers argued that the crustal-derived melts were transported to the overlying mantle wedge and reacted with the lithospheric mantle peridotite of the North China Craton (e.g., Zhao et al. 2012; Li et al. 2016). *P–T–t* conditions for the partial melting were constrained to be generally at 3.5–2.0 GPa and ~800 °C at 230–220 Ma (e.g., Wang et al. 2014, 2017).

After suturing of the two Cratons during the Triassic, the Sulu belt and central to eastern parts of the North China Craton were reactivated from *c.* 180 Ma due to shallow-angle subduction of the paleo-Pacific oceanic plate (Engebretson et al. 1985; Maruyama et al. 1997; Mao et al. 2011; Van der Meer et al. 2012). Subsequently in the Late Jurassic to Early Cretaceous (*c.* 145 Ma), the paleo-Pacific plate changed its velocity vector to the northeast, with the convergence direction subparallel to the entire continental margin of eastern Asia (Engebretson et al. 1985; Maruyama et al. 1997). The northern extension of this convergent plate boundary caused large-scale sinistral strike-slip structures in eastern China, such as the Tan-Lu fault system (Xu and Zhu 1994). In addition, extensive magmatism and gold mineralization were developed in eastern China, including Shandong, Hebei and Liaoning provinces, during the period of plate subduction and subsequent slab rollback (e.g., Wang et al. 1998; Yang et al. 2003; Zheng et al. 2018), indicating a possible petrogenetic relationship between these tectono-magmatic thermal events and the convergence of the paleo-Pacific plate. Numerous studies have established the geochronological framework of these Late Mesozoic intrusions and volcanic rocks, which were mainly produced during two episodes: Late Jurassic (*c.* 160–145 Ma) and Early Cretaceous (*c.* 140–110 Ma; Zhao et al. 2013). The Late Jurassic magmatic rocks are dominantly granites with minor amounts of mafic to andesitic rocks that mainly occur in the eastern part of the Sulu belt, Jiaobei terrane and Liaodong peninsula (e.g., Wu et al. 2005). In comparison, the Early Cretaceous magmatic rocks show greater variation in rock types and crop out throughout the entire Sulu belt and the central to eastern parts of the North China Craton (e.g., Zhao et al. 2013; Zheng et al. 2018).

This study focuses on a suite of andesite dykes that occurs at General's Hill within the central Sulu UHP belt (Fig. S1; e.g., the eastern part of one dyke is also shown in Fig. 2 of Wang et al. 2017). The outcrop at General's Hill extends along

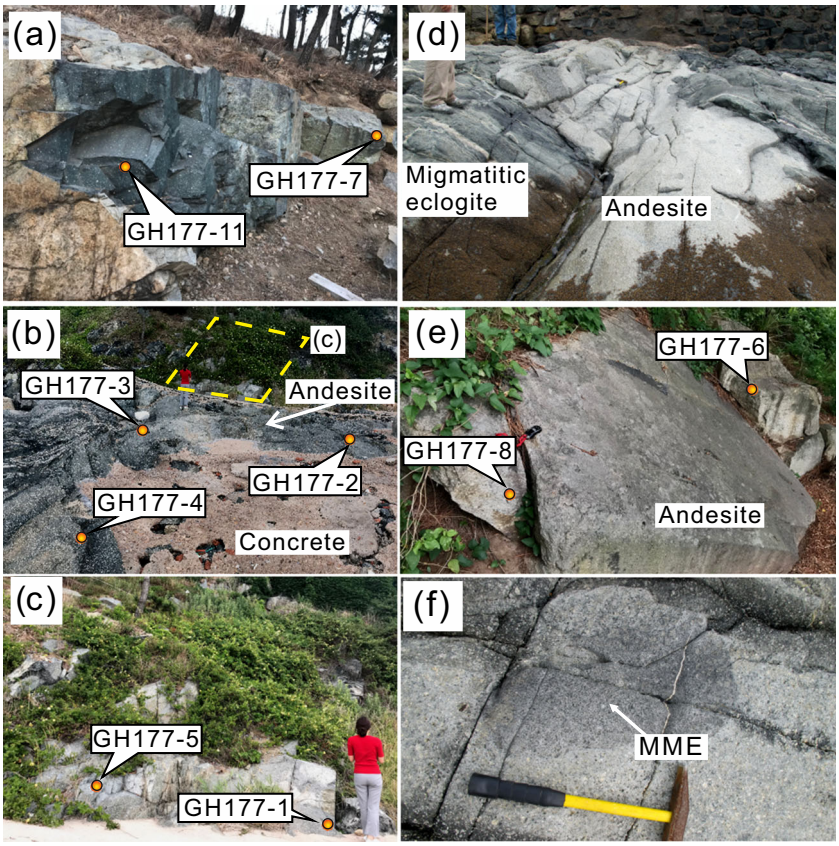

Fig. 2 Field relations of the andesite dykes with sample locations marked by orange colored circles; MME: mafic microgranular enclave. **a**–**e** occurrence of the four representative fresh andesite dykes that hosted by migmatitic eclogite; **f** oval MME in andesite

the coast for more than 1 km with a width of 50–100 m, where it basically consists of strongly foliated, tight to isoclinally folded migmatitic UHP eclogite, surrounded by granite gneiss (the northern part of the outcrop was shown in Wang et al. 2014, 2017). All the units are cut by Laoshan granite plutons and minor lamprophyre, andesite and granite porphyry dykes. The andesite dykes are ~2–20 m in width with exposed lengths of ~5–30 m (Fig. 2a–e). They are fresh and show clear chilled margins with the host eclogite; occasionally mafic microgranular enclaves are present within the andesite (Fig. 2f). The andesite has typical porphyritic textures; the phenocrysts (~30–40 vol.%) are mainly composed of plagioclase, hornblende and clinopyroxene, with minor amounts of finer-grained magnetite (Fig. 3). The plagioclase phenocrysts are lath-shaped and form euhedral–subhedral grains with long axis sizes up to ~1 cm across (Fig. 3a–d). Some plagioclase grains have abundant cracks, and are commonly altered by epidote, wairakite and clay minerals such as kaolinite and sericite (Fig. 3b and c). The hornblende forms subhedral to anhedral phenocrysts up to 1 mm in diameter; it commonly contains fine-grained apatite, titanite and magnetite as inclusions (Fig. 3e). The clinopyroxene phenocrysts with abundant cracks are euhedral–anhedral with long axis sizes up to ~3 mm, and commonly contain inclusions of magnetite and titanite (Fig. 3f–h). In most cases, they are surrounded by thin rims of hornblende (Fig. 3f–h). The matrix (~60–70 vol.%) mainly consists of fine-grained quartz and K-feldspar, with minor amounts of biotite, magnetite, titanite, apatite and zircon. Since all the andesites show similar features in the field, twelve unaltered andesite samples from different dykes were chosen for this study (Figs. S1 and 2). Using the petrological, geochemical and geochronological dataset created from these samples, we investigate the petrogenesis of these andesites, and discuss their implications for recycling of crustal materials into the ancient SCLM during continental/oceanic subduction.

Analytical methods

Mineral major element compositions

Major element compositions of minerals were measured using the JEOL JXA-8230 electron microprobe analyzer (EPMA) at the Center for Global Tectonics at School of Earth Sciences, China University of Geosciences (CUG), Wuhan. Operating conditions were as follows: 15 kV accelerating voltage, 20 nA cup current, 1 μm beam diameter, and 10 s counting time on peak and 5 s on background. A series of natural and synthetic standards from SPI (Structure Probe, Inc.) company was used, including: orthoclase for K; diopside for Ca; magnetite for Fe; jadeite for Na; pyrope for Mg; Yttrium Al garnet for Al; albite for Si; rutile for Ti; Apatite for P; pentilandite for Ni; rhodonite

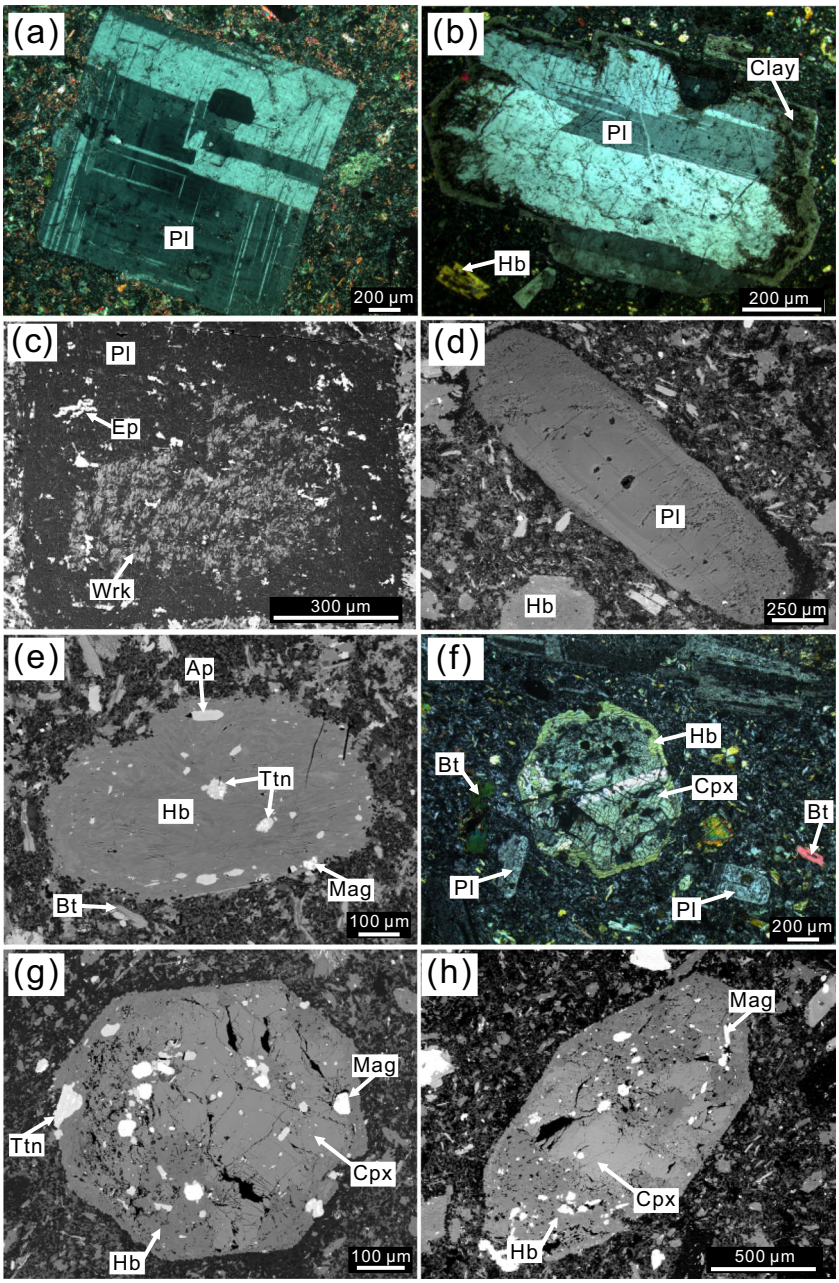

Fig. 3 Photomicrographs of major minerals and the microstructures of andesite. Cross-polarized light (**a**, **b**) and back-scattered electron (BSE; **c**, **d**) images to show the microstructure of plagioclase phenocrysts that are lath-shaped and in parts show altered cores (**c**), and which are commonly surrounded by clay minerals (b). The plagioclase phenocrysts often show clear zoning (**d**). BSE image of a hornblende phenocryst (**e**) that contains various inclusions such as Ap, Ttn and magnetite. Cross-polarized light (**f**) and BSE images (**g**, **h**) of clinopyroxene phenocrysts altered by variable amounts of hornblende. Abbreviations of mineral names are after Whitney and Evans (2010)

for Mn; chromite for Cr. Na, K and P were analyzed first to reduce electron beam-induced loss. Raw data were corrected using a ZAF algorithm (where Z = element atom number, A = X-ray absorption, F = X-ray fluorescence; Heinrich et al. 1986).

Mineral trace element compositions

Trace element compositions of major phenocryst phases including plagioclase, hornblende and clinopyroxene were measured using the laser ablation inductively coupled plasma-mass spectrometry (LA-ICP-MS) at the Wuhan Sample Solution Analytical Technology Co., Ltd., Wuhan, China. Detailed operating conditions for the laser ablation system and the ICP-MS instrument and data reduction are similar to those described by Zong et al. (2017). Laser sampling was performed using a GeolasPro laser ablation system that consists of a COMPexPro 102 ArF excimer laser (wavelength of 193 nm and maximum energy of 200 mJ) and a MicroLas optical system. An Agilent 7700e ICP-MS instrument was used to acquire ion-signal intensities. Helium was applied as a carrier gas. Argon was used as the make-up gas and mixed with the carrier gas via a T-connector before entering the ICP. A "wire" signal smoothing device is included in this laser ablation system (Hu et al. 2015). The spot size and frequency of the laser were set to 44 μm and 5 Hz, respectively. Trace

element compositions of minerals were calibrated against various reference materials (BHVO-2G, BCR-2G, BIR-1G and NIST SRM610) without using an internal standard (Liu et al. 2008a). The measured and recommended values of the standards are provided in Table S1. Measuring conditions of each analysis were approximately 20 s of background acquisition, followed by 50 s data acquisition from the sample. An Excel-based software *ICPMSDataCal* was used to perform off-line selection and integration of background and analyzed signals, time-drift correction and quantitative calibration for trace element analysis (Liu et al. 2008a).

Whole-rock major and trace element analysis

Fresh rock samples free of visible alteration were crushed in a corundum jaw crusher to <60 mesh. For each sample, approximately 70 g was further powdered in an agate ring mill to <200 mesh for whole-rock major oxide, trace element and Sr–Nd isotope analyses. Major oxides were determined at the Comprehensive Rock and Mineral Test Center, Wuhan. For the major elements, H_2O^+ and CO_2 were determined by gravimetry, while other oxides were measured using conventional X-ray fluorescence (XRF) spectrometry (Shimadzu XRF-1800). The analytical uncertainty is generally <5 %. Trace element concentrations were analyzed at the State Key Laboratory of Geological Processes and Mineral Resources (GPMR), CUG, Wuhan using an Agilent 7500a ICP-MS. International standards including AGV-2, BHVO-2, BCR-2 and RGM-2 were used as reference materials (associated results of the standards and recommended values are summarized in Table S2). The detailed sample digestion procedure for ICP-MS analysis, and the analytical precision and accuracy for trace elements follow those described by Liu et al. (2008b).

Whole-rock Sr–Nd isotope analysis

Whole-rock Sr and Nd isotope compositions were also acquired at the State Key Laboratory of GPMR, CUG, Wuhan, using a Neptune Plus multi-collector (MC) ICP-MS. $^{87}Rb/^{86}Sr$ and $^{147}Sm/^{144}Nd$ ratios were calculated from Rb–Sr and Sm–Nd concentrations measured by ICP-MS, respectively. The measured Sr and Nd isotope ratios were normalized to $^{86}Sr/^{88}Sr = 0.1194$ (Nier 1938) and $^{146}Nd/^{144}Nd = 0.7219$ (O'Nions et al. 1977), respectively. During the measurement, the NBS987 and Chinese GBW04411 standards gave an average $^{87}Sr/^{86}Sr$ value of 0.710274 ± 0.000008 (2σ) and 0.759909 ± 0.000006 (2σ), respectively, while the BCR-2 and JNdi-1 standards yielded an average $^{143}Nd/^{144}Nd$ of 0.512592 ± 0.000003 (2σ) and 0.512119 ± 0.000008 (2σ), respectively. Detailed sample preparation, chemical separation and analytical procedures for Sr–Nd isotope analysis are similar to those given by Gao et al. (2004).

Zircon U–Pb dating, trace element and Lu–Hf isotope analysis

Zircon was separated from samples following conventional crushing, sieving, heavy liquid and magnetic separation procedures. Individual zircon grains for analysis were separated from any remaining contaminant minerals under a binocular microscope. For each sample, a selection of the zircon separate was mounted in an epoxy resin block and polished to approximately half thickness for analysis. In order to monitor the surface and internal structures of the zircons, back-scattered electron and cathodoluminescence (CL) images were acquired using a FEI Quanta 450 field emission gun scanning electron microscope equipped with a Gatan Mono CL4+ CL system at the State Key Laboratory of GPMR, CUG, Wuhan. The operating conditions were 10 kV acceleration voltages and a spot size of 5 μm with a working distance of 13.9–14.1 mm.

Zircon U–Pb isotope and trace element compositions were determined synchronously by LA-ICP-MS at the State Key Laboratory of GPMR, CUG, Wuhan; working conditions and the data reduction protocol follow those described by Liu et al. (2008a). Samples were ablated using a GeoLas 2005 system (spot size of 32 μm), which was connected to an Agilent 7500a ICP-MS instrument to acquire ion-signal intensities. Each analysis was subjected to a background acquisition of approximately 20 s followed by 50 s data acquisition from the unknowns. Zircon 91500 was used as external standard for U–Pb dating, and was analyzed twice bracketing each batch of 6 unknown samples. U–Th–Pb isotopic ratios used for zircon 91500 during the measurement are from Wiedenbeck et al. (1995). Uncertainty of the preferred values was propagated to the ultimate results of the samples. Trace element compositions of zircons were calibrated against multiple-reference materials (BCR-2G and BIR-1G) without applying internal standardization (Liu et al. 2008a). The preferred values of element concentrations for the USGS reference glasses are from the GeoReM database (http://georem.mpch-mainz.gwdg.de/). Off-line selection and integration of background and analytical signals, and time-drift correction and quantitative calibration for U–Pb dating and trace element analysis were performed by *ICPMSDataCal* (Liu et al. 2008a). The data were processed using the program *ISOPLOT/Ex_ver3* developed by Ludwig (2003).

After zircon U–Pb and trace element analysis, in-situ Lu–Hf isotope analysis of zircon was carried out using a Neptune Plus MC-ICP-MS in combination with a Geolas 2005 excimer ArF laser ablation system at the State Key Laboratory of GPMR, CUG, Wuhan. All Lu–Hf isotope analyses were acquired in single spot ablation mode with a spot size of 44 μm at the location of the same spots used for dating. Each measurement was done using a background acquisition of 20 s, followed by 50 s of signal acquisition from the unknowns.

Zircon 91500, GJ-1 and Temora were used as reference standards, the results of which are given in Table S3. Detailed operating conditions for the laser ablation system and the MC-ICP-MS instrument, and the analytical method are the same as used by Hu et al. (2012). Mass bias of Hf and Yb were calculated using an exponential correction law and normalized values of $^{179}Hf/^{177}Hf = 0.7325$ and $^{173}Yb/^{171}Yb = 1.1248$ (Blichert-Toft et al. 1997), respectively. Interference of ^{176}Yb on ^{176}Hf and ^{176}Lu on ^{176}Hf were corrected by measuring the interference-free ^{173}Yb and ^{175}Lu isotopes and using the recommended ratios of $^{176}Yb/^{173}Yb = 0.7876$ (McCulloch et al. 1977) and $^{176}Lu/^{175}Lu = 0.02656$ (Blichert-Toft et al. 1997), respectively. A decay constant of 1.867×10^{-11} year^{-1} for ^{176}Lu was chosen for data calculation (Söderlund et al. 2004). $\varepsilon_{Hf}(t)$ values were calculated relative to a chondritic reservoir with a $^{176}Hf/^{177}Hf$ ratio of 0.282772 and $^{176}Lu/^{177}Hf$ of 0.0332 (Blichert-Toft and Albarède 1997). Single-stage Hf model ages were calculated relative to a model depleted mantle with a present day $^{176}Hf/^{177}Hf$ ratio of 0.28325 and a $^{176}Lu/^{177}Hf$ ratio of 0.0384 (Vervoort and Blichert-Toft 1999). Two-stage Hf model ages were calculated by using a mean $^{176}Lu/^{177}Hf$ ratio of 0.015 for the average continental crust as suggested by Griffin et al. (2002).

Analytical results

Mineral major and trace element compositions

Representative major element compositions of phenocrysts (including plagioclase, hornblende and clinopyroxene) and matrix minerals (K-feldspar, biotite and titanite) are given in Table S4. In Table S5, trace element compositions of plagioclase, hornblende and clinopyroxene are summarized.

Plagioclase

Plagioclase is the most abundant phenocryst in the andesite. It contains low amounts of K-feldspar component ($An_{28-42}Ab_{57-69}Kfs_{1-6}$). In the An–Ab–Kfs diagram, plagioclase mainly plots in the andesine field of the classical plagioclase nomenclature (Fig. 4a). In general plagioclase phenocrysts are weakly zoned (e.g., Fig. 3d); two representative grains from sample GH177–2 were selected to check their major and trace element variations (Fig. S2). As illustrated in Fig. S2a–d, the plagioclases show a zoning as expected from magmatic crystallization; CaO decreases and Na_2O increases from core to rim, corresponding to ~An_{40} in the cores and ~An_{30} in the rims. However, the REE contents don't show considerable variations within a single phenocryst and also between the two grains studied (∑REE =47.42–63.17 ppm vs. 43.18–58.31 ppm). Chondrite-normalized plots show consistent REE patterns that are characterized by an enrichment in LREE [$(La/Sm)_N = 21.66–52.35$] but deleption in H-(Heavy-) REE [$(Gd/Yb)_N = 0.82–14.91$] with pronounced positive Eu anomalies ($Eu/Eu^* = 9.91–24.44$; Fig. S2e, f).

Hornblende and actinolite

Hornblende occurs as phenocryst or alteration rim surrounding clinopyroxene. The hornblende phenocrysts contain variable amounts of SiO_2 (50.33–56.68 wt.%), FeO_t (10.29–14.34 wt.%), CaO (11.66–12.38 wt.%) and MgO (12.99–17.24 wt.%) (Table S4). According to the Hawthorne et al. (2012) nomenclature, the hornblende phenocrysts belong to the subgroup of calcium amphiboles and for convenience were displayed in the Leake et al. (1997) diagram, which show that the respective analyses plot in the magnesiohornblende to actinolite fields (Fig. 4b). On the other hand, alteration rims of amphibole surrounding clinopyroxene have similar SiO_2 (52.84–55.77 wt.%) and CaO (11.93–12.41 wt.%), and relatively lower FeO_t (8.51–11.08 wt.%) but higher MgO (16.10–18.35 wt.%) contents in comparison with those of the phenocrysts (Table S4). Based on the classification of Leake et al. (1997), the compositions of these late amphiboles plot in the actinolite field (Fig. 4b). Two single hornblende phenocrysts from sample GH177–2 were chosen to study major and trace element profiles, in order to check if there are any compositional variations present. As illustrated in Fig. S3, the oxides of SiO_2, FeO, MgO and CaO however show very flat profiles.

For trace element compositions, the analyzed two hornblende phenocrysts have equally low total REE concentrations (∑REE = 5.10–10.30 ppm, except for two outliers at 21.69 ppm and 44.57 ppm, respectively) compared to the actinolite rims (∑REE = 20.53–41.52 ppm) surrounding clinopyroxene (Table S5). The hornblende phenocrysts show consistent chondrite-normalized REE patterns that are depleted in LREE [$(La/Sm)_N = 0.15–0.59$, with two outliers at 1.96 and 2.40] and flat to slightly enriched in HREE [$(Gd/Yb)_N = 0.48–1.10$, with two outliers at 2.06 and 1.24] generally with negative Eu anomalies ($Eu/Eu^* = 0.41–1.15$; Fig. S4a–d), except for two LREE-enriched spots (i.e. the two outliers as described above), possibly resulting from contamination of tiny LREE-rich mineral inclusions. In primitive mantle-normalized multi-element diagrams (Fig. S4b, d), the both hornblende phenocrysts show pronounced positive anomalies of Th, U, Nd and Pb. Compared to the phenocrysts, the alteration rims of actinolite show depletion both in LREE and HREE [$(La/Sm)_N = 0.14–0.54$; $(Gd/Yb)_N = 1.78–2.06$] with negligible to negative Eu anomalies ($Eu/Eu^* = 0.27–0.87$; Fig. S4e). They show positive anomalies of Th, U, Pb and Nd but negative anomalies of Ta and Sr in a primitive mantle-normalized multi-element diagram (Fig. S4f).

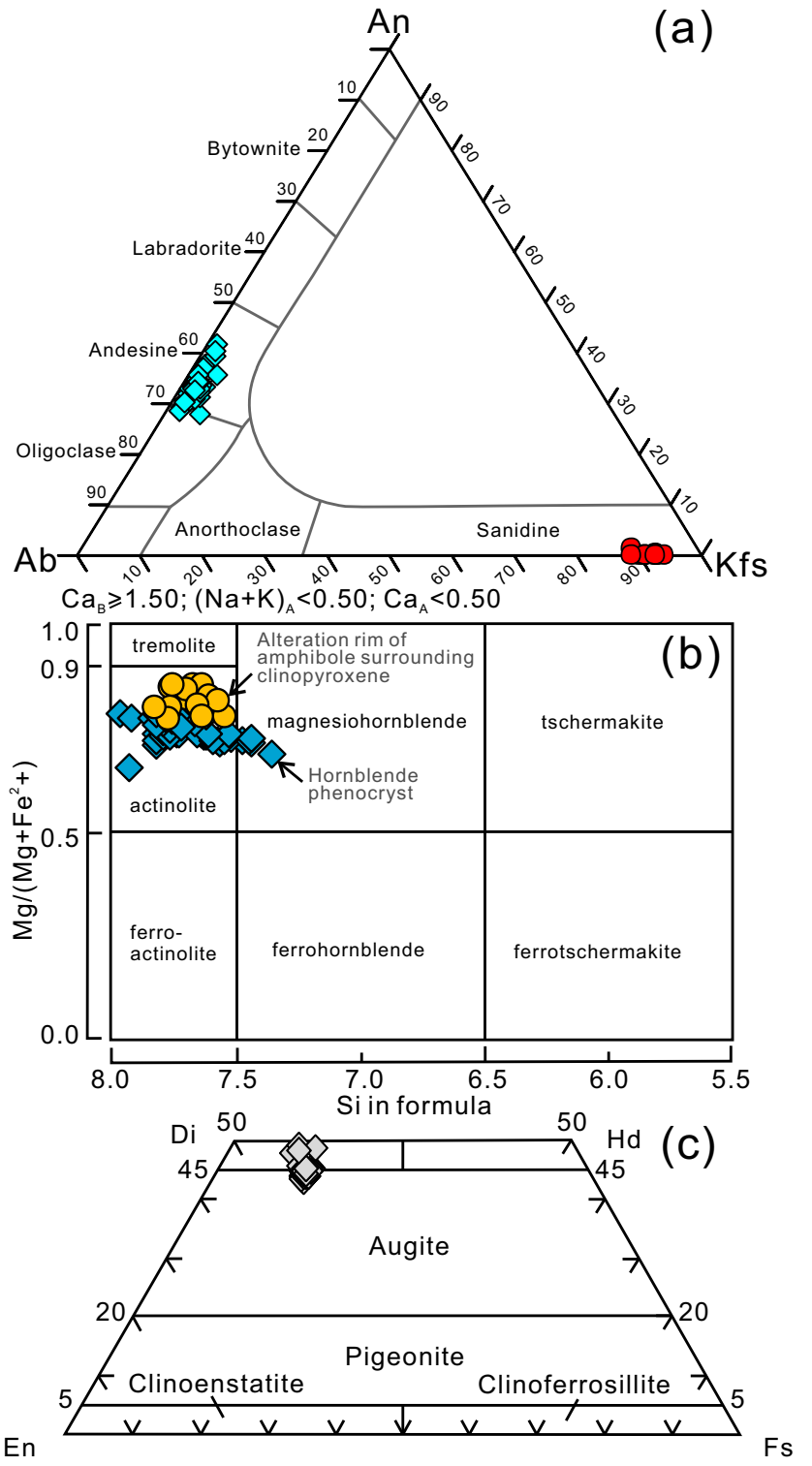

Fig. 4 **a** An–Ab–Kfs triangular diagram (modified after Deer et al. 1963) showing the compositions of plagioclase phenocrysts (blue squares) and K-feldspar in the matrix (red dots); **b** classification of calcic hornblende phenocrysts (blue diamonds) and alteration rims (orange dots) of amphibole surrounding clinopyroxene after Leake et al. (1997); **c** classification of clinopyroxene phenocrysts after Morimoto (1988)

Clinopyroxene

The clinopyroxene phenocrysts are relatively high in SiO_2 (53.47–55.02 wt.%), FeO_t (6.06–8.59 wt.%) and CaO (20.47–23.63 wt.%), but low in MgO (13.83–14.91 wt.%), Al_2O_3 (0.23–1.34 wt.%) and TiO_2 (from below detection limit to 0.23 wt.%) with high Mg# values [Mg# = 100 × Mg/(Mg + Fe^{2+}) molar] of 74–81. Moreover, the clinopyroxene is homogeneous in major element compositions within a single grain (Fig. S5a, b). In the enstatite–ferrosilite–diopside–hedenbergite quadrilateral diagram after Morimoto (1988), the compositions plot in the diopside ($Wo_{45–49}En_{39–43}Fs_{10–}$

$_{14}$) and augite ($Wo_{43–44}En_{42–43}Fs_{13–14}$) fields (Fig. 4c). The clinopyroxene phenocrysts have moderate REE abundances (∑REE = 151.86–264.13 ppm) and exhibit flat chondrite-normalized LREE [$(La/Sm)_N$ = 0.72–1.06] and depleted HREE [$(Gd/Yb)_N$ = 1.69–2.25] patterns with conspicuous negative Eu anomalies (Eu/Eu^* = 0.44–0.64; Fig. S5c). In a primitive mantle-normalized spider diagram, they are enriched in Th and U but depleted in Nb, Ta, Zr and Hf (Fig. S5d).

Matrix minerals

K-feldspar in the matrix is mainly composed of SiO_2 (64.66–66.03 wt.%), Al_2O_3 (17.36–18.16 wt.%) and K_2O (14.38–15.99 wt.%), with minor amounts of FeO_t (0.04–0.17 wt.%), CaO (from below detection limit to 0.04 wt.%) and Na_2O (0.68–1.24 wt.%); they possess low albite content ($Kfs_{88–94}Ab_{6–11}$; Fig. 4a). In the An–Ab–Kfs diagram, they mainly plot in the sanidine field (Fig. 4a). Biotite has relatively consistent compositions of SiO_2 (36.00–37.91 wt.%), FeO_t (18.45–19.29 wt.%), Al_2O_3 (12.42–13.62 wt.%), MgO (11.12–12.53 wt.%) and K_2O (8.92–10.06 wt.%), with minor TiO_2 (0.04–0.17 wt.%) and Na_2O (0.68–1.24 wt.%). Titanite mainly comprises of SiO_2 (30.62–31.11 wt.%), TiO_2 (37.55–38.62 wt.%) and CaO (27.22–28.74 wt.%) with a chemical formula of $Ca_{0.970–1.016}Ti_{0.931–0.965}Si_{1.011–1.021}O_5$.

Whole-rock major oxides, trace elements and Sr–Nd isotope compositions

Twelve andesite samples were analyzed for major and trace element compositions, which are summarized in Table S6 and presented in Figs. S6, 5 and 6. They possess moderate concentrations of SiO_2 (54.97–62.24 wt.%), $Na_2O + K_2O$ (6.35–7.24 wt.%), Al_2O_3 (13.32–14.70 wt.%), MgO (3.37–7.12 wt.%), Ni (37–107 ppm) and Cr (124–360 ppm) with high Mg# values of 54–64 (Fig. S6). They mainly fall in the field of andesite on the Nb/Y vs. Zr/TiO_2 ratio diagram (Fig. 5a; Winchester and Floyd 1977). In the total alkalis vs. silica diagram (TAS), the samples plot in the field of trachyandesite, with one exception that plots in the field of basaltic trachyandesite (Fig. 5b) and on a diagram of K_2O vs. SiO_2 (Fig. 5c), the andesites fall in the field of high-K calc-alkaline to shoshonite series.

On a chondrite-normalized diagram (Fig. 6a), the andesites are characterized by enriched LREE patterns relative to HREE [$(La/Yb)_N$ = 16.72–19.91], with weak to negligible Eu anomalies (Eu/Eu^* = 0.83–0.97). In a primitive mantle-normalized multi-element diagram (Fig. 6b), they show pronounced enrichment in LILE, but depletion in HFSE. Both diagrams prove nearly identical patterns of all studied andesite samples.

Nine andesite samples (GH177–1 to GH177–9) were further analyzed for whole-rock Sr–Nd isotope compositions, as listed in Table S7. Initial $^{87}Sr/^{86}Sr$ ratios and $\varepsilon_{Nd}(t)$ values were corrected to t = 120 Ma, according to the results of zircon U–Pb dating reported below. The andesites exhibit variably high initial $^{87}Sr/^{86}Sr$ ratios of 0.7073–0.7086 and negative $\varepsilon_{Nd}(t)$ values of −15.7 to −14.4 (Fig. 7), yielding two-stage Nd model ages of 2088–2188 Ma.

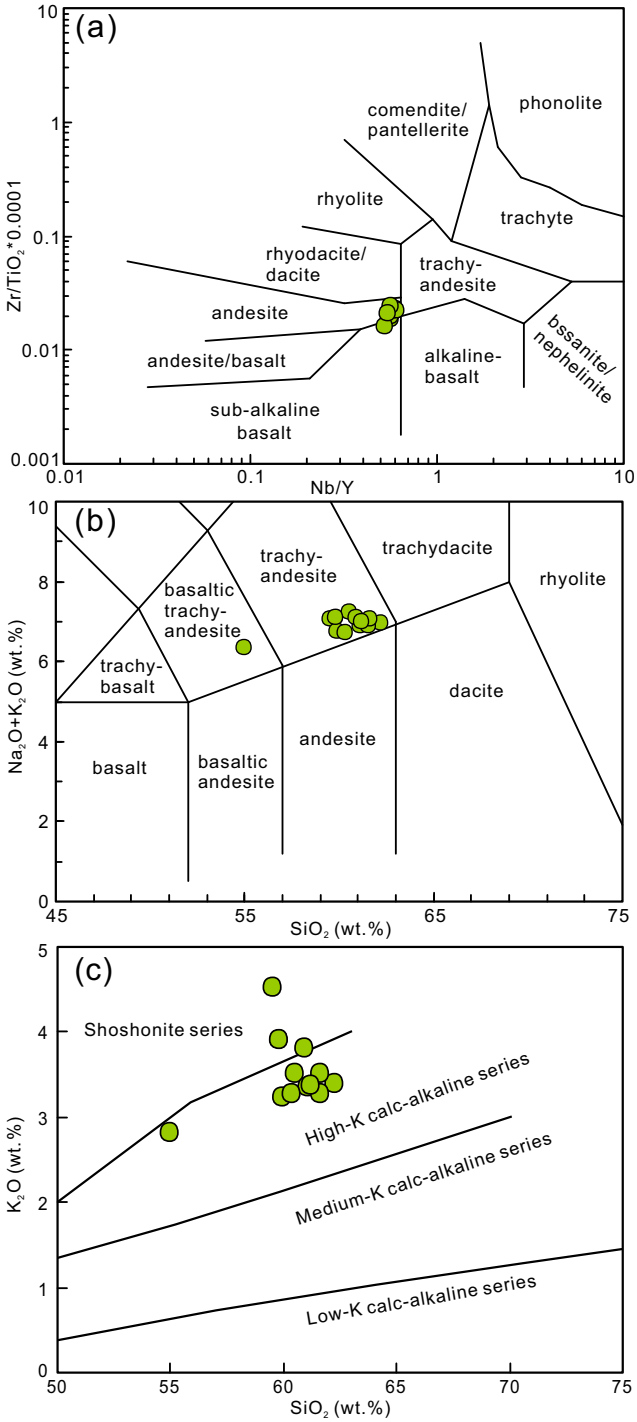

Fig. 5 $Zr/TiO_2 \times 0.0001$ vs. Nb/Y chemical classification after Winchester and Floyd (1977) (**a**), $Na_2O + K_2O$ vs. silica (TAS, **b**) diagram after Le Maitre (2002), and SiO_2 vs. K_2O diagram (**c**; after Morrison 1980; Peccerillo and Taylor 1976) for the andesites at General's Hill

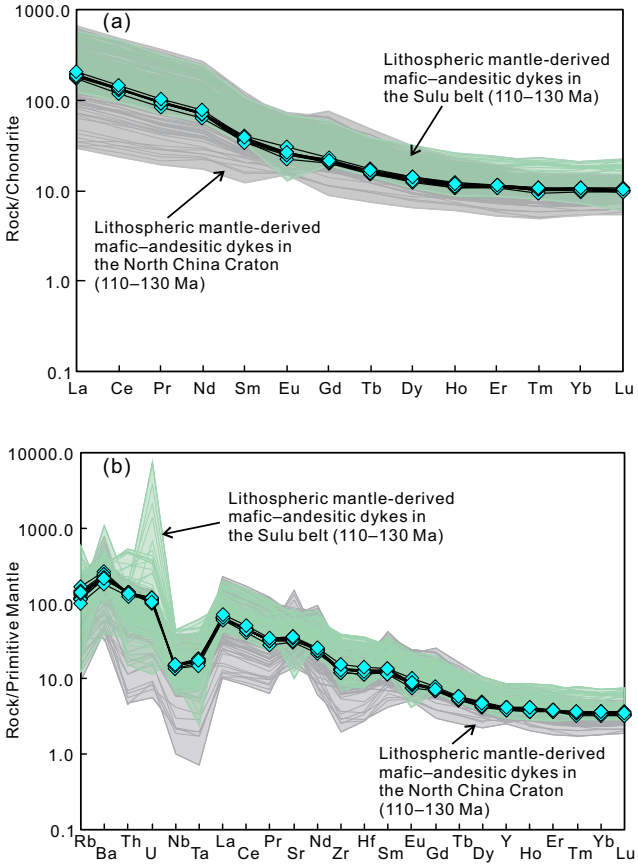

Fig. 6 Whole-rock chondrite-normalized rare earth element patterns (**a**), and primitive mantle-normalized trace element patterns (**b**) of the andesites at General's Hill. Data from contemporaneously crystallized lithospheric mantle-derived mafic–andesitic igneous rocks in the Sulu belt and the interiors of North China Craton are shown for comparison. Data sources: Fan et al. 2001; Zhang et al. 2002, 2012; Guo et al. 2004, 2005, 2014a, b; Xu et al. 2004b; Yang et al. 2005, 2008, 2012; Liu et al. 2006, 2008, 2009, 2012; Yang and Li 2008; Tang et al. 2009; Pei et al. 2011; Ma et al. 2014a, b; Cai et al. 2015; Deng et al. 2017. Normalization values are from Sun and McDonough (1989)

Zircon U–Pb dating and trace elements

Zircon from four andesite samples (GH177–1, −3, −8 and −12) was analyzed for U–Pb dating and trace element compositions, as summarized in Tables S8 and S9, respectively. The zircon grains, most of which have isometric to long prismatic forms, are generally euhedral, colorless and transparent in plane light. They have grain lengths ranging from 50 to 300 μm, with length to width ratios of 1:1–5:1. In CL images, most grains show oscillatory or banded zoning with moderate luminescence, but in some cases inherited zircons can be observed (Fig. 8). Some grains are partially resorbed or recrystallized and show thin metamorphic rims (Fig. 8a), suggesting modification by post-magmatic high-temperature hydrothermal alteration (cf. Liati et al. 2002; Zhang et al. 2012).

Thirty-six analyses were performed on 36 grains for sample GH177–1. One analysis on an inherited zircon gives a Neoproterozoic $^{206}Pb/^{238}U$ age of 645 ± 18 Ma, while the other 35 spots on newly crystallized magmatic zircon domains with high Th/U ratios (0.85–2.71) yield concordant $^{206}Pb/^{238}U$ ages between 122 ± 6 and 111 ± 7 Ma with a weighted mean age of 116 ± 1 Ma (2σ, MSWD = 1.9; Fig. 9a). Twenty-seven spots were analyzed for sample GH177–3, among which 26 analyses show Th/U ratios of 0.79–1.51 and give $^{206}Pb/^{238}U$ ages from 130 ± 6 to 108 ± 6 Ma yielding a weighted mean age of 119 ± 2 Ma (2σ, MSWD = 5.8; Fig. 9b). One analysis on a relict zircon gives an Archean $^{207}Pb/^{206}Pb$ age of 3292 ± 48 Ma (Fig. 9b). Similarly, twenty-seven analyses of sample GH177–8 were studied, and 25 spots yield a weighted mean age of 119 ± 2 Ma (2σ, MSWD = 4.9); the other 2 spots give Paleoproterozoic and Neoproterozoic ages of 2354 ± 76 and 780 ± 19 Ma, respectively (Fig. 9c). Seventeen analyses performed for sample GH177–12 give concordant $^{206}Pb/^{238}U$ ages from 133 ± 4 to 118 ± 3 Ma, with a weighted mean age of 124 ± 2 Ma (2σ, MSWD = 4.4; Fig. 9d).

Taken together, the analyses on newly crystallized magmatic zircon domains of all the andesite samples studied yield consistent Early Cretaceous U–Pb ages of 124 ± 2 to 116 ± 1 Ma, whereas the relict zircons give variable Neoproterozoic (780 ± 19 and 645 ± 18 Ma), Paleoproterozoic (2377 ± 46) and Archean (3165 ± 38 Ma) ages.

As illustrated in Fig. 9e–h, both magmatic and relict zircon domains from all the four samples possess similar trace element compositions. They have variably high total REE concentrations (∑REE = 444–4182 ppm, mostly >1500 ppm) with variable but in general low Hf/Y ratios (3.43–22.75). In chondrite-normalized REE plots they show steep HREE patterns [$(Dy/Yb)_N$ = 0.10–0.23] with pronounced negative Eu anomalies (Eu/Eu* = 0.11–0. 77, mostly <0.50).

Zircon Lu–Hf isotope compositions

A total of 32 analyses on both magmatic and relict zircon domains from three samples (GH177–1, −3 and − 8) was performed to determine Lu–Hf isotope compositions. The results are listed in Table S10 and graphically processed in Fig. 10. The $\varepsilon_{Hf}(t)$ values and Hf model ages are corrected to t = 120 Ma for magmatic zircon and to the apparent ages for relict zircon, based on the U–Pb dating results as reported above.

For sample GH177–1, the magmatic zircon domains (n = 7) have restricted Hf isotopic compositions with $^{176}Hf/^{177}Hf$ ratios of 0.281940–0.282021 and $\varepsilon_{Hf}(t)$ values of −26.9 to −24.0, corresponding to two-stage Hf model ages of 2681–2863 Ma; one analysis on a relict zircon (645 Ma) yields an $\varepsilon_{Hf}(t)$ value of −17.7 and a two-stage Hf model age of 2681 Ma (Fig. 10a and b). For sample GH177–3, the magmatic zircons (n = 11) exhibit $\varepsilon_{Hf}(t)$ values of −26.3 to −17.6, corresponding to two-stage Hf

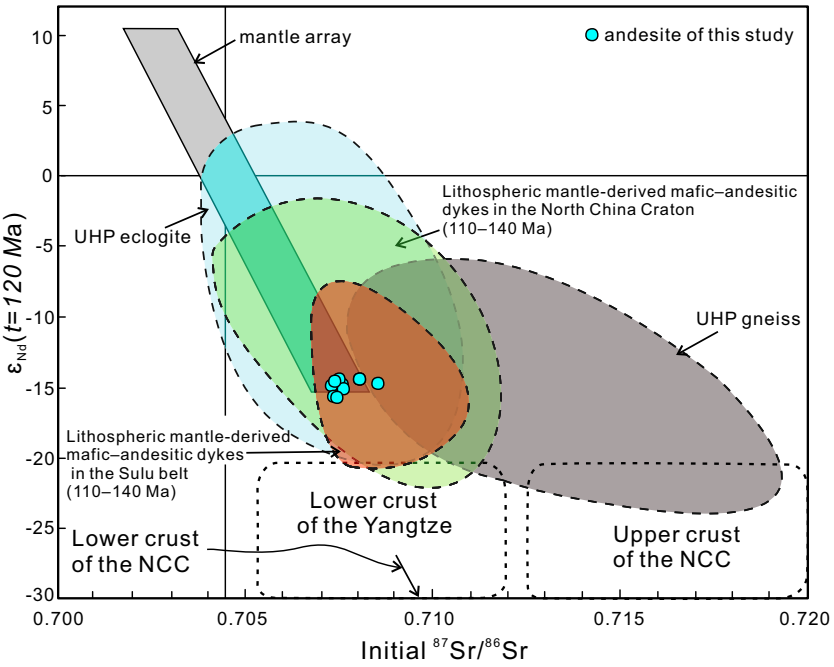

Fig. 7 $\varepsilon_{Nd}(t)$ vs. initial $^{87}Sr/^{86}Sr$ plot at $t = 120$ Ma for the andesites (cyan dots) at General's Hill. Sr–Nd compositions of UHP eclogite (light blue area) and gneiss (grey area) in the Sulu belt, and contemporaneous lithospheric mantle-derived mafic–andesitic igneous rocks in the Sulu belt (light red area) and in the North China Craton (light green area) are also plotted for comparison (also calculated back to $t = 120$ Ma). Data sources for the UHP eclogite and gneiss are: Chen et al. 2002, 2014b; Zhao et al. 2007; Tang et al. 2008; Wang et al. 2017; Data sources for the andesitic–mafic igneous rocks are the same as those in Fig. 6; lower crust of the Yangtze Craton, lower and upper crust of the NCC (North China Craton) are from Jahn et al. (1999)

model ages of 2282–2838 Ma, while one available analysis on a relict zircon (3292 Ma) yields a less negative $\varepsilon_{Hf}(t)$ value of −4.2 and an older two-stage Hf model age of 3860 Ma (Fig. 10c and d). Similarly, the magmatic zircon domains ($n = 10$) in sample GH177–8 have negative $\varepsilon_{Hf}(t)$ values of −27.0 to −23.8, yielding two-stage Hf model ages of 2121–2871 Ma; relict zircons at apparent ages of 2354 and 780 Ma exhibit less negative $\varepsilon_{Hf}(t)$ values of −8.1 and −7.1, respectively, corresponding to two-stage Hf model ages of 3380 and 2121 Ma (Fig. 10e and f).

Discussion

Timing of crystallization

Most zircon grains in the andesites show clear oscillatory zoning, variably high Th/U ratios (0.50–2.71, with a median value of 1.14), and steep HREE patterns with obvious negative Eu anomalies (Figs. 8 and 9; Table S8 and S9), typical of magmatic origin (cf. Pidgeon 1992; Hoskin and Ireland 2000; Du et al. 2017a, b; Rubatto 2017). The LA-ICP-MS U–Pb dating

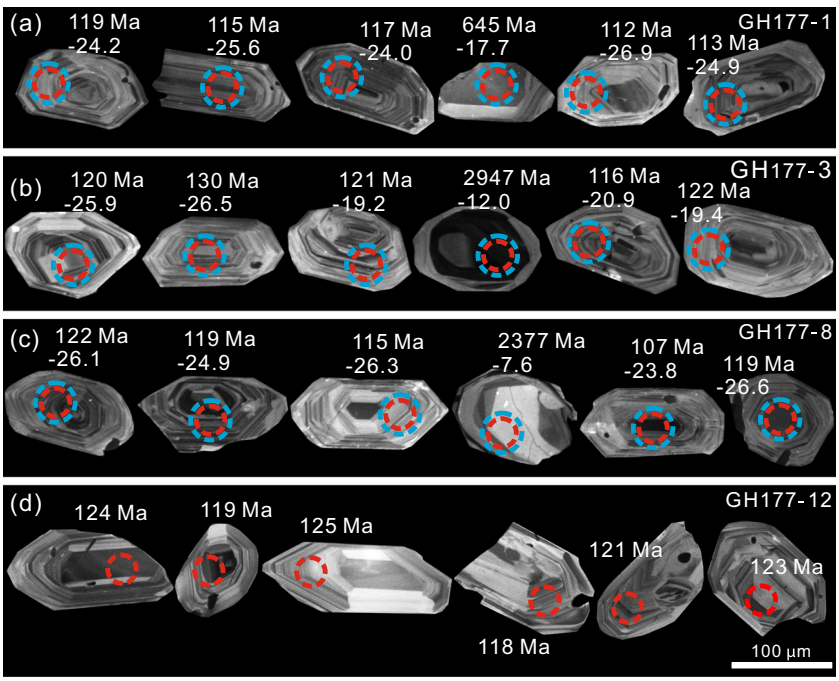

Fig. 8 Cathodoluminescence images of representative zircon grains from four andesite samples. Circles mark the locations of LA-ICP-MS U–Pb (red) and Hf isotope (blue) analyses, respectively, together with corresponding $^{206}U/^{238}Pb$ dates and $\varepsilon_{Hf}(t)$ values

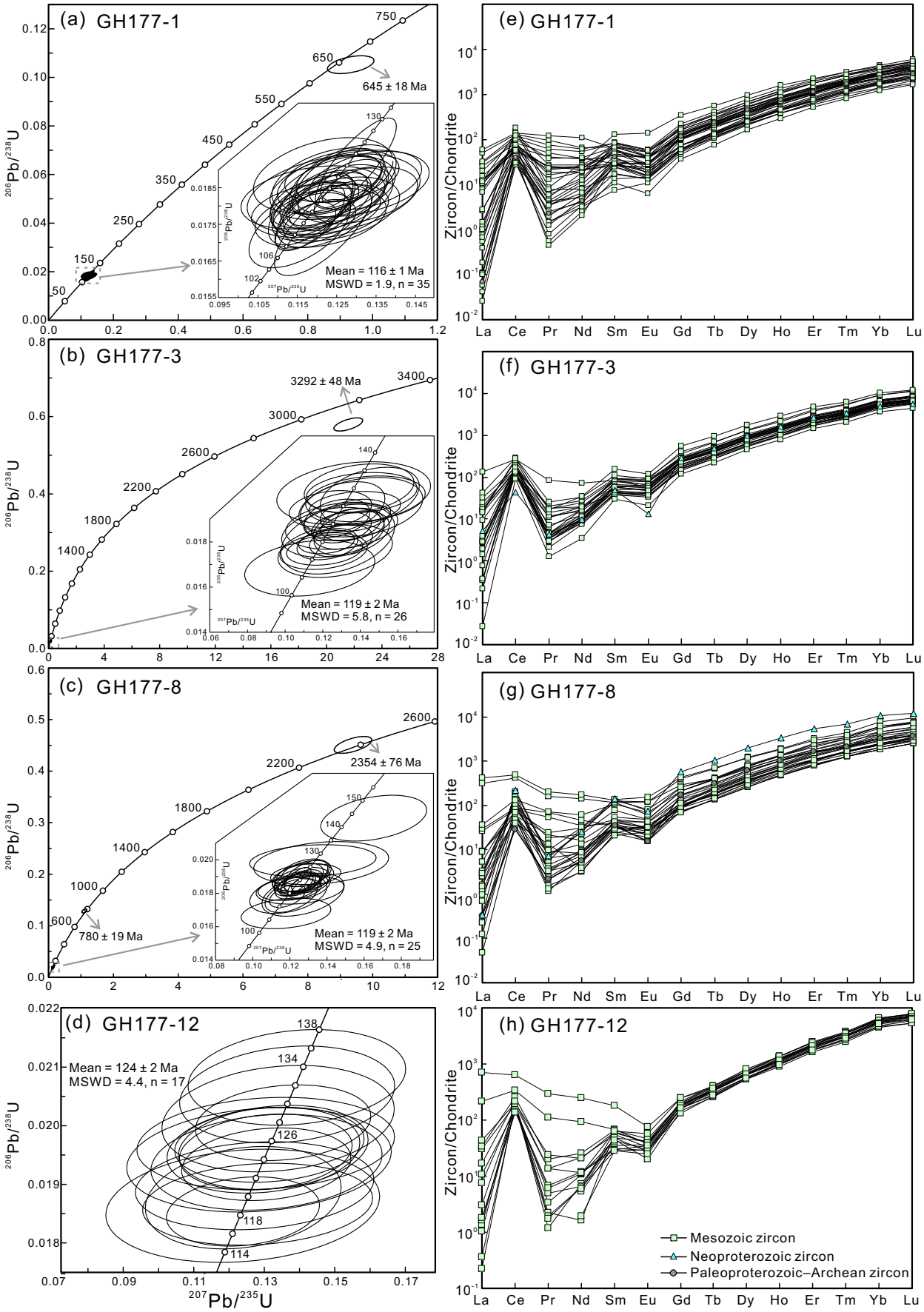
(a) GH177-1
645 ± 18 Ma
Mean = 116 ± 1 Ma
MSWD = 1.9, n = 35
(b) GH177-3
3292 ± 48 Ma
Mean = 119 ± 2 Ma
MSWD = 5.8, n = 26
(c) GH177-8
2354 ± 76 Ma
780 ± 19 Ma
Mean = 119 ± 2 Ma
MSWD = 4.9, n = 25
(d) GH177-12
Mean = 124 ± 2 Ma
MSWD = 4.4, n = 17
206Pb/238U
207Pb/235U
(e) GH177-1
(f) GH177-3
(g) GH177-8
(h) GH177-12
Zircon/Chondrite
La Ce Pr Nd Sm Eu Gd Tb Dy Ho Er Tm Yb Lu
Mesozoic zircon
Neoproterozoic zircon
Paleoproterozoic–Archean zircon

◀ **Fig. 9** U–Pb concordia plots (**a**–**d**) and chondrite-normalized REE patterns (**e**–**h**) of zircons from the andesites. The insets in **a**–**c** are U–Pb concordia diagrams for concordant new zircon domains; the mean $^{206}Pb/^{238}U$ ages are reported with 2σ uncertainty. Normalization values are from Sun and McDonough (1989)

on these magmatic zircons yielded consistent ages of 124 ± 2 to 116 ± 1 Ma (Fig. 9a–d). These ages are in line with data of the timing of extensive magmatism in the Dabie–Sulu orogen and in the adjacent continental margin of the North China Craton during the Early Cretaceous (cf. Liu et al. 2009; Zhao et al. 2013). Therefore, we interpret the ages of 124–116 Ma as crystallization ages, thus dating the eruption of andesitic lava at General's Hill.

Source nature of the andesite

As summarized in Table S6, the andesites have intermediate concentrations of MgO (3.37–7.12 wt.%), Ni (37–107 ppm) and Cr (124–360 ppm) with high Mg# values of 54–64, different from those crystallized from crustal-derived melts (Cr = 4.49–21.1 ppm; Mg# values = 15–54, with two exceptions of 56 and 58, respectively; cf. Patiño Douce and Beard 1995; Rapp and Watson 1995; Qian and Hermann 2013). In addition, the clinopyroxene phenocrysts exhibit high Mg# values of 74–81 (Table S4), also indicating crystallization from a mantle source (cf. Liang et al. 2018). Accordingly, they are interpreted to be generated from mantle-derived magmas of ultramafic to mafic lithologies. However, except for Cr and Ni contents, the studied andesites exhibit distinct features of trace elements and radiogenic isotopes that resemble those of the continental crust (Taylor and McLennan 1995), including: (1) arc-like trace element patterns with enrichment of LILE and LREE but depletion of HFSE (Fig. 6); (2) high initial $^{87}Sr/^{86}Sr$ ratios and pronounced negative whole-rock $\varepsilon_{Nd}(t)$ and zircon $\varepsilon_{Hf}(t)$ values (Figs. 7 and 10); and (3) enrichment of Th and U but depletion of Nb, Ta, Zr and Hf for the hornblende and clinopyroxene phenocrysts (Figs. S4 and S5). These features indicate that the mantle source can neither be the normal asthenospheric mantle nor a mid-ocean ridge-type mantle that are isotopically depleted (e.g., Hofmann 1988; Song et al. 2018). In this regard, in view of the tectonic setting where the andesite occurs and the evolutional history of this region, the most appropriate candidate for the mantle source is the SCLM of the North China Craton, which was fertile in compositions due to incorporation of crustal components. The andesites are enriched in LILE and contain relatively high amounts of K_2O (2.81–4.52 wt.%), implying a potassium-

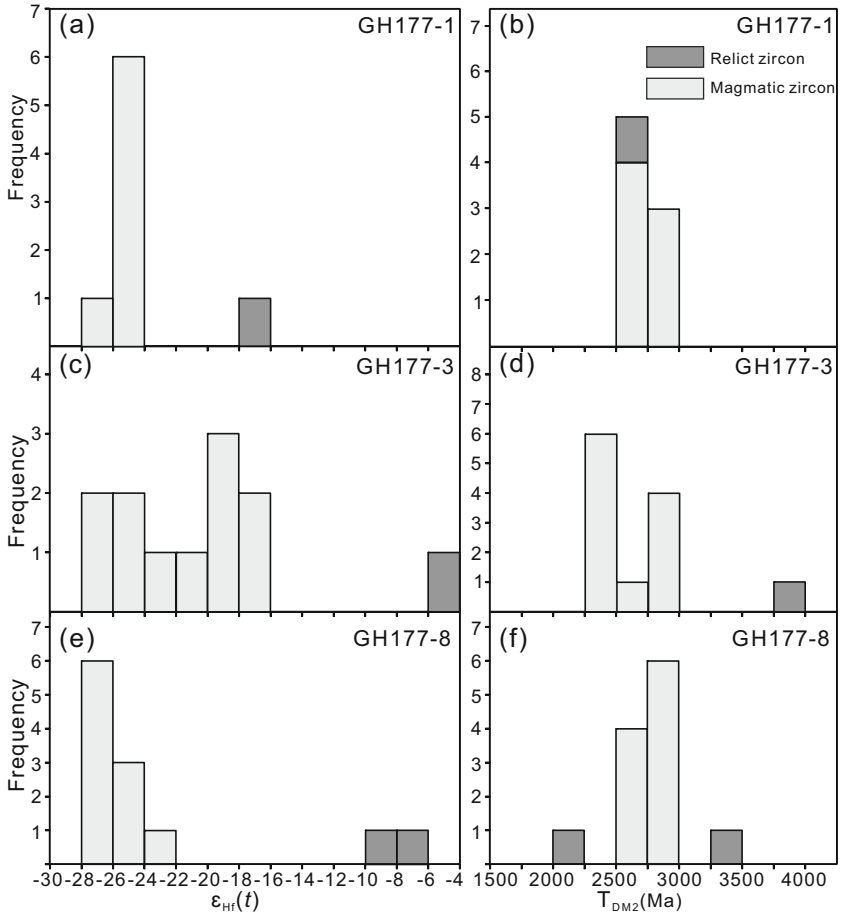

Fig. 10 Histograms of zircon $\varepsilon_{Hf}(t)$ values (**a**, **c**, **e**) and two-stage Hf model ages (**b**, **d**, **f**) for the andesites at General's Hill

bearing (with minerals such as hornblende and phlogopite) mantle source for their origin (Foley et al. 1996; Ionov et al. 1997). These rocks have Rb/Sr and Ba/Rb ratios of 0.09–0.16 and 16.25–21.77, respectively, which plot in the phlogopite field in the Rb/Sr vs. Ba/Rb diagram after Furman and Graham (1999) (Fig. S7), indicating a predominance of phlogopite over hornblende in the melting source.

How did the crustal materials be incorporated into the mantle-derived magmas?

When and how did the crustal material become incorporated into the mantle source generating andesitic magmatism? Answers to these questions are essential to decipher the petrogenesis of the andesites. In general, during ascent of mantle-derived magmas en route to the surface through the continental crust, they might be contaminated by crustal materials (e.g., AFC process). However, as demonstrated in Figs. 7 and 10, the andesites have a limited range of whole-rock initial $^{87}Sr/^{86}Sr$ and $\varepsilon_{Nd}(t)$ as well as zircon $\varepsilon_{Hf}(t)$ values. This argues against the possibility of significant crustal contamination during ascent of the mantle-derived magmas through the continental crust. On the other hand, although the andesites exhibit a relatively narrow range of MgO concentrations, Al_2O_3, $Na_2O + K_2O$ and SiO_2 decrease but FeO_t and CaO increase with the increase of MgO (Fig. S6). This indicates that slight fractional crystallization of clinopyroxene and/or hornblende could have occurred during magma ascent. Moreover, plagioclase phenocrysts exhibit pronounced positive Eu anomalies, while the hornblende and clinopyroxene exhibit weak to moderate negative Eu anomalies (Figs. S2, S4 and S5), suggesting that plagioclase fractionation did occur during the evolution of the parent magma. However, consistently low contents of TiO_2 (0.64–0.83 wt.%) in these rocks do not match fractionation of Fe–Ti oxides. The weak normal zoning of major elements of plagioclase may largely reflect simple growth history during cooling. Nevertheless, fractional crystallization cannot contribute to enriched signatures of isotope compositions if the andesites were derived from a depleted mantle source. Therefore, it is inferred that the andesites inherited their geochemical features from the melting source that was metasomatized by crustal materials through source mixing prior to the onset of andesitic magmatism (cf. Zhao et al. 2013; Chen et al. 2014a). The inferred existence of phlogopite and/or hornblende in the melting source also calls for a fertile mantle that was metasomatized by fluids/melts.

With respect to the process of source mixing for the Mesozoic igneous rocks in the Dabie–Sulu orogen, the prevailing model considered is that, which involves deep continental subduction of the Yangtze Craton and subsequent crust–mantle interactions in a continental subduction channel (e.g., Zheng 2012; Zhao et al. 2013; Dai et al. 2016). This model was proposed mainly based on the following observations (cf. Zhao et al. 2013; Dai et al. 2016; Li et al. 2016): (1) the igneous rocks, including basalt, hornblendite, lamprophyre, diabase and andesites, commonly contain relict zircons of Neoproterozoic and Triassic ages, resembling those of the UHP metamorphic rocks from the Yangtze Craton; (2) the igneous rocks have enriched isotope compositions (including Sr, Nd, Pb, Hf and O) that are similar to the host UHP gneiss and eclogite in this region; (3) mantle-derived orogenic peridotites in the Dabie–Sulu orogen have crust-like elemental and isotopic signatures; they contain metasomatic zircons also of Neoproterozoic and Triassic ages. The andesites at General's Hill have relict zircons that yield Neoproterozic, Paleoproterozoic and Archean U–Pb ages (Fig. 9a–c), similar to the prominent ages dated from the UHP metamorphic rocks in the Dabie–Sulu orogen and the crustal rocks of the North China Craton, respectively (Zheng et al. 2005; Hacker et al. 2006; Liu and Liou 2011). Since crustal contamination was negligible in this case, these relict zircons should not be physically incorporated into the magma during its ascent. In this regard, the above mentioned geochemical and geochronological features indicate involvement of crustal rocks from both the Yangtze and North China Cratons into the SCLM by source mixing during the Triassic orogeny. On the other hand, as summarized in Table S11 and shown in Fig. 11, contemporaneously formed mafic–andesitic igneous rocks (140–110 Ma) with similar geochemical features not only crop out in the Dabie–Sulu orogen, they also occur in western Shandong, Liaoning peninsula and even at several localities in the central–western domains of the North China Craton, including the Taihang mountain, Beijing region and Jining area of Inner Mongolia (cf. Chen et al. 2003; Guo et al. 2014b; Zhang et al. 2014; Zheng et al. 2018). The Triassic continental subduction may not count for the fertilization of the SCLM and generation of the Early Cretaceous igneous rocks in the interiors of the North China Craton. As a consequence, a more common geodynamic mechanism is further called for to decode the Mesozoic magmatism in the vast regions of eastern China.

The andesites at General's Hill and lithospheric mantle-derived mafic–andesitic rocks of Early Cretaceous ages in eastern China share similar arc-like geochemical features (Fig. 6). They share similarities with typical island-arc basalts and andesites above oceanic subduction zones, such as the classical Andean subductioin zone and the Japanese Islands (Perfit et al. 1980; Stern and Kilian 1996; Kelemen et al. 2003a, b). These characteristics point towards a similar process of formation. Geophysical observations and large-scale numerical modeling data demonstrate that subduction of the paleo-Pacific plate played a dominant role in the mantle dynamics of eastern China during the Late Mesozoic (*c.* 150–90 Ma; Niu 2005; Seton et al. 2012; Kusky et al. 2014).

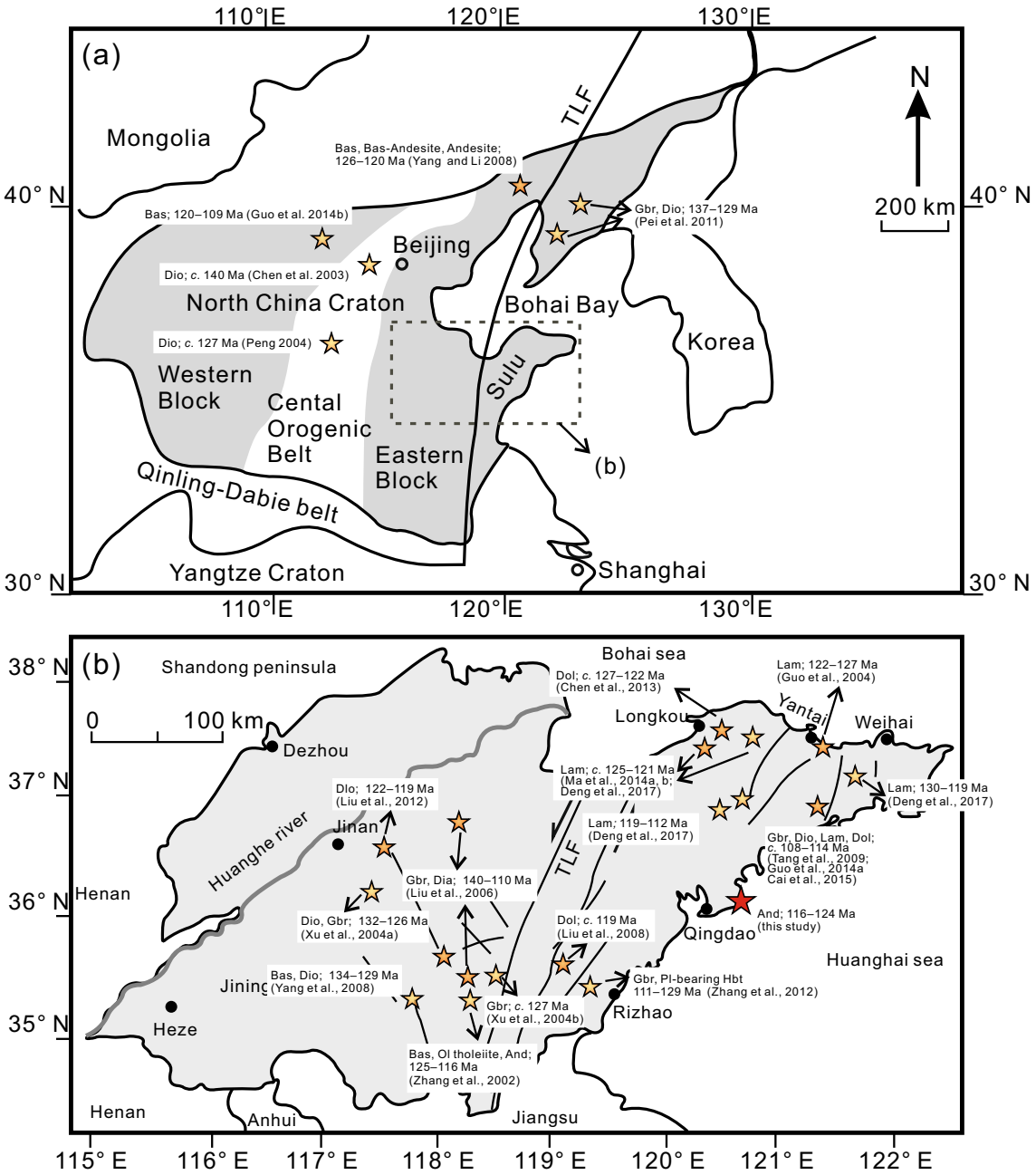

Fig. 11 Spatial distribution of representative lithospheric mantle-derived mafic–andesitic igneous rocks of Early Cretaceous ages (*c.* 140–110 Ma) in eastern China, including the Sulu orogenic belt and the interiors of the North China Craton (modified after Liu et al. 2006). For the igneous rocks exposed in Shandong peninsula, spatial and chronological distribution information is shown in enlarged Fig. 11b. The yellow stars denote the location of each study, with specification of age information and literature source, while the red star represents the results of this study. TLF: Tan-Lu Fault; Lam: Lamprophyre; Dio: Diorite; Dol: Dolerite; Dia: Diabase; Gbr: Gabbro; And: Andesite; Pl-bearing Hbt: Plagioclase-bearing Hornblendite; Bas: Basalt; Data sources: Zhang et al. 2002, 2012; Chen et al. 2003; Guo et al. 2004, 2014a, b; Peng 2004; Xu et al. 2004a, b; Liu et al. 2006, 2008, 2009, 2012; Yang et al. 2008; Yang and Li 2008; Tang et al. 2009; Pei et al. 2011; Ma et al. 2014a, b; Cai et al. 2015; Deng et al. 2017

Therefore, in addition to the metasomatic process during the Triassic orogeny, the subduction of paleo-Pacific plate along the eastern margin of Asian continent could be considered as another appropriate candidate for the fertilization of the SCLM beneath the North China Craton. Note that the andesites contain high initial $^{87}Sr/^{86}Sr$ ratios, significantly negative $\varepsilon_{Nd}(t)$ values and zircon $\varepsilon_{Hf}(t)$ values, which imply that the metasomatic fluids/melts were mainly released from marine sediments that were located on top of the subducted oceanic crust.

Petrogenesis of the andesite

Although more and more studies have confirmed the genetic link of andesite formation with plate subduction and crust–mantle interactions in a subduction channel, there are still open questions related to its genesis (e.g., as reviewed by Gómez-Tuena et al., 2014). Two contrasting models, namely the basalt-input model and the andesite-input model, were proposed to the andesite formation (e.g., Hildreth and Moorbath 1988; Gómez-Tuena et al. 2014). The major characteristics of the alternative models refer to either a crystallization of primary andesitic melts from slab and/or mantle materials, or to a derivative andesitic product of a basaltic magma that differentiated in the continental crust. Below, we firstly evaluate the possibility of a differentiation from basaltic melts to form the andesite and then we focus on questions related to its petrogenesis.

As illustrated in Fig. 11, contemporaneous mafic–andesitic igneous rocks, including basalt, lamprophyre, spessartite, kersantite, gabbro, dolerite, hornblendite and monzodiorite, with similar elemental and isotopic features (Figs. 6 and 7), are widely exposed in the Sulu belt and the adjacent continental crust of the North China Craton (e.g., Guo et al. 2004; Wu et al. 2005; Zhao et al. 2013; Ma et al. 2014a, b; Cai et al. 2015; Deng et al. 2017; Zheng et al. 2018). This suggests an interrelation between these rocks and indicates the probability

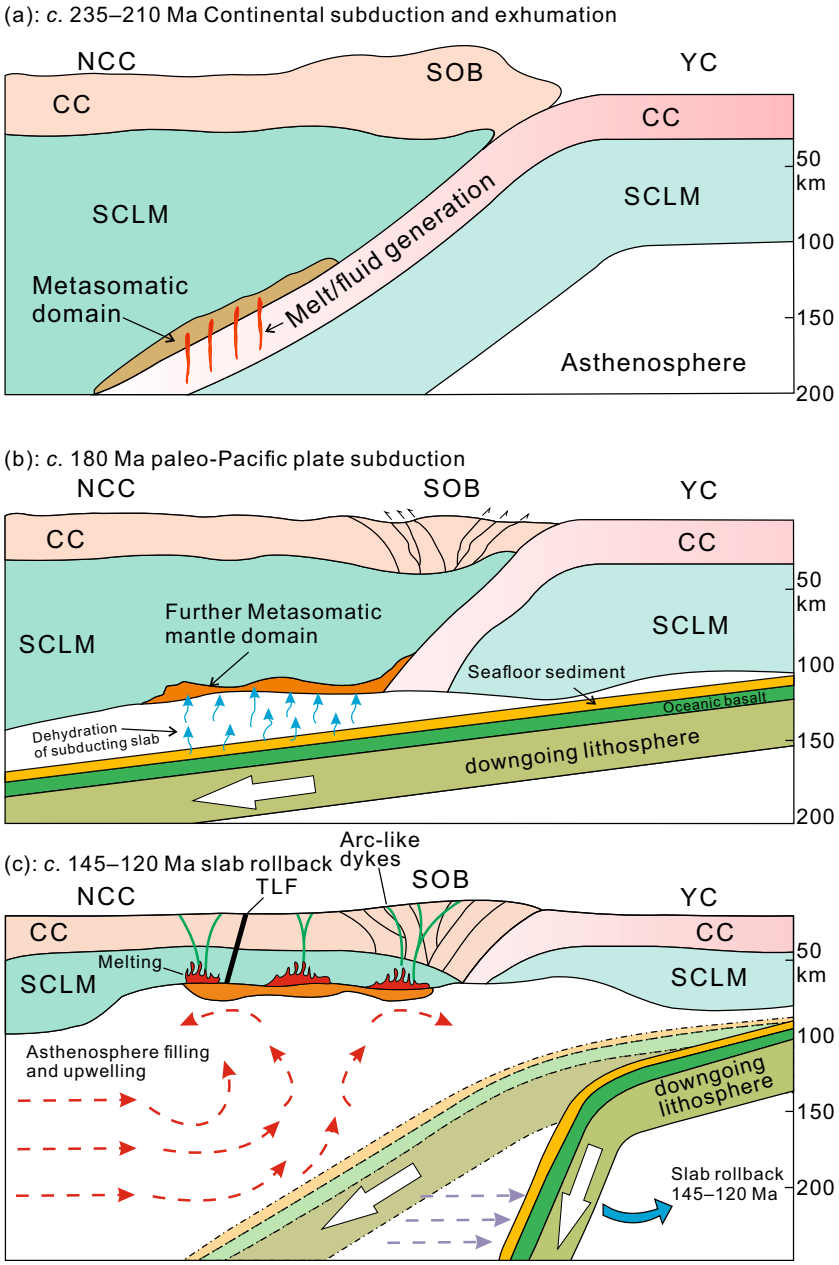

Fig. 12 Geological sketch diagrams to illustrate the chronological development of subduction and the related genesis of arc-like andesites and contemporaneous mafic rocks in eastern China (modified from Deng et al. 2017). **a** Deep continental subduction of the Yangtze Craton beneath the North China Craton during the Triassic, generating ultrahigh-pressure metamorphic rocks. During the subduction and exhumation, melts and fluids were generated and penetrated into the overlying SCLM; **b**, **c** Subdcution of the paleo-Pacific plate further metasomatized the SCLM that was then melted due to slab rollback, resulting in the development of the andesitic magmatism. See text for further interpretation. SCLM: subcontinental lithospheric mantle; NCC: North China Craton; YC: Yangtze Craton; SOB: Sulu Orogenic Belt; CC: Continental Crust; TLF: Tan-Lu Fault

that the andesites represent evolved products of melts that originally yielded a basaltic composition. However, as shown in Fig. S6, there are no clear common features related to major and trace elements vs. MgO interrelation between these rocks and the studied andesites, indicating that fractional crystallization of basaltic magmas did not play a significant role in the andesite formation. In fact, the andesite at General's Hill is crosscut by lamprophyre dykes (Fig. S1), which also suggests that it was not derived from the parent basaltic magmas that crystallized the lamprophyre. Therefore, the vast occurrences of Early Cretaceous mafic to andesitic igneous rocks in the Sulu belt and in the interiors of the North China Craton are characterized to originate from heterogeneous sources due to variable degrees of crustal metasomatism, and the andesites essentially crystallized from primary andesitic melts.

Based on integrated geochemical and geochronological studies of andesite from the Luzong basin in the Middle–Lower Yangtze River Belt of southern China, Chen et al. (2014a) proposed a two-stage process to account for the genesis of orogenic andesites that occur above oceanic subduction zones. These authors argue that mantle-wedge peridotite firstly reacted with slab-derived melts/fluids during the subduction of an oceanic crust, giving rise to fertile and enriched metasomatites of ultramafic to mafic compositions; the metasomatites were subsequently melted to generate andesitic magmatism. In view of the similarity in geochemical characteristics between these rocks and the studied andesites and the tectonic evolution of this region, a similar scenario is also applicable to illustrate the generation of andesitic magmas at General's Hill, as illustrated in the geological sketch drawings of Fig. 12. In detail, the SCLM wedge beneath the North China Craton was firstly modified by hydrous melts/fluids mostly released from the subducted continental crust of the Yangtze Craton during the Triassic (Fig. 12a; *c.* 240–220 Ma). The subducted slab might also have brought crustal fragments from the North China Craton into the subduction zone, resulting in the existence of relict zircons in the andesites with Neoproterozoic, Paleoproterozoic and Neooarchean ages. Since the Jurassic (Fig. 12b; *c.* 180 Ma), paleo-Pacific plate started to subduct beneath the Eurasian continent at a shallow angle (e.g., Engebretson et al. 1985; Maruyama et al. 1997). The slab-derived fluids/melts, mostly from marine sediments, were transported to the overlying mantle wedge and further reacted with the SCLM peridotite to form metasomatic rocks of ultramafic to mafic compositions (cf. Kelemen et al. 2003a, b). The subducted paleo-Pacific slab then progressively rolled back from *c.* 145 to 120 Ma, which would not only cause lithospheric extension, but also result in flux of asthenospheric mantle materials to the 'gap' between old and new slab positions (Niu 2005; Kusky et al. 2014; Zheng et al. 2018). This process would provide the needed heat for partial melting of the overlying enriched mantle and the formation of andesitic magmas (Fig. 12c).

Conclusions

This study of Early Cretaceous andesites in the Sulu UHP belt provides new insights that contribute to our understanding of how an ancient SCLM was metasomatized and reactivated in a complicated terrane that underwent both continental and oceanic subduction. The crystallization age of the andesites at General's Hill which erupted at 124 to 116 Ma, is coeval with the large-scale mafic magmatism in the Dabie–Sulu orogen and in the interiors of the North China Craton. The andesites contain intermediate amounts of SiO_2, MgO, Ni and Cr with high Mg# values, and are characterized by arc-like trace element patterns with enriched whole-rock Sr–Nd and zircon Hf isotope compositions. The hornblende and clinopyroxene phenocrysts show enrichment of Th and U but a pronounced depletion of HFSE, such as Nb and Zr. These features indicate that they were originated from an enriched mantle source of mafic–ultramafic compositions. Relict zircons of Neoproterozoic, Paleoproterozoic and Archean ages and two-stage Nd and zircon Hf model ages of Paleoproterozoic to Neoarchean Era may indicate involvement of crustal rocks from both the Yangtze and North China Cratons into the SCLM by source mixing during the Triassic orogeny. However, a comprehensive lateral comparison of contemporaneously formed mafic–andesitic rocks with the studied andesites reveals that the source rocks were further metasomatized by reactions of SCLM-wedge peridotite with fluids/melts released from subducted marine sediments at the slab–mantle interface during the paleo-Pacific plate subduction in the Jurassic to Cretaceous. Slab rollback and accompanied asthenospheric mantle upwelling are considered as the favored geodynamic mechanisms for the generation of extensive mafic to andesitic magmatism in the Sulu belt of eastern China.

Acknowledgements This work was supported by the National Natural Science Foundation of China (Nos. 41803031, 41230960 and 41572044), the Natural Science Foundation of Shandong Province (ZR2018BD019) and the Project funded by China Postdoctoral Science Foundation (No. 2017 M622232). We thank J.P. Wang and B.W. Ning for help with EPMA analysis, Z.C. Hu and K.Q. Zong for help with LA(MC)-ICP-MS zircon analysis, and L. Zhou for help with whole-rock Sr–Nd isotope analysis. We acknowledge editorial advice from Maarten A.T.M. Broekmans and Shah Wali Faryad, and detailed and constructive comments from Vladislav Rapprich and Alessandro Fabbrizio that greatly contributed to the improvement of the paper.

References

Altherr R, Holl A, Hegner E, Langer C, Kreuzer H (2000) High-potassium, calc-alkaline I-type plutonism in the European Variscides: northern Vosges (France) and northern Schwarzwald (Germany). Lithos 50(1–3):51–73

Annen C, Blundy JD, Sparks RSJ (2005) The genesis of intermediate and silicic magmas in deep crustal hot zones. J Petrol 47(3):505–539

Blichert-Toft J, Albarède F (1997) The Lu–Hf isotope geochemistry of chondrites and the evolution of the mantle–crust system. Earth Planet Sci Lett 148:243–258

Blichert-Toft J, Chauvel C, Albarède F (1997) Separation of Hf and Lu for high-precision isotope analysis of rock samples by magnetic sector-multiple collector ICP-MS. Contrib Mineral Petrol 127: 248–260

Cai YC, Fan HR, Santosh M, Hu FF, Yang KF, Hu Z (2015) Subduction-related metasomatism of the lithospheric mantle beneath the south-eastern North China craton: evidence from mafic to intermediate dykes in the northern Sulu orogen. Tectonophysics 659:137–151

Cao YT, Liu L, Chen DL, Wang C, Yang WQ, Kang L, Zhu XH (2017) Partial melting during exhumation of Paleozoic retrograde eclogite in north Qaidam, western China. J Asian Earth Sci 148:223–240

Chen B, Ye K, Liu JB (2002) Cogenetic relationship of the Yangkou gabbro-to-granite unit, Su-Lu terrane, eastern China, and implications for UHP metamorphism. J Geol Soc 159(4):457–467

Chen B, Jahn BM, Zhai MG (2003) Sr–Nd isotopic characteristics of the Mesozoic magmatism in the Taihang–Yanshan orogen, North China craton, and implications for Archean lithosphere thining. J Geol Soc Lond 160:963–970

Chen L, Zhao ZF, Zheng YF (2014a) Origin of andesitic rocks: geochemical constraints from Mesozoic volcanics in the Luzong basin, South China. Lithos 190:220–239

Chen YX, Zheng YF, Li L, Chen RX (2014b) Fluid–rock interaction and geochemical transport during protolith emplacement and continental collision: a tale from Qinglongshan ultrahigh-pressure metamorphic rocks in the Sulu orogen. Am J Sci 314(1):357–399

Chopin C (2003) Ultrahigh-pressure metamorphism: tracing continental crust into the mantle. Earth Planet Sci Lett 212(1):1–14

Dai FQ, Zhao ZF, Dai LQ, Zheng YF (2016) Slab–mantle interaction in the petrogenesis of andesitic magmas: geochemical evidence from postcollisional intermediate volcanic rocks in the Dabie Orogen, China. J Petrol 57(6):1109–1134

Deer WA, Howie RA, Zussman J (1963) Rock-Forming Minerals (Vol. 4 Framework Silicates). Longmans, Green and Co Ltd, London (435pp)

Deng J, Liu XF, Wang QF, Dilek Y, Liang YY (2017) Isotopic characterization and petrogenetic modeling of early cretaceous mafic diking—lithospheric extension in the North China craton, eastern Asia. GSA Bull 129(11–12):1379–1407

Du QX, Han ZZ, Shen X, Gao L, Han M, Song Z, Li JJ, Zhong WJ, Yan JL, Liu H (2017a) Geochemistry and geochronology of upper Permian–upper Triassic volcanic rocks in eastern Jilin Province, NE China: implications for the tectonic evolution of the Palaeo-Asian Ocean. Int Geol Rev 59(3):368–390

Du QX, Han ZZ, Shen X, Han C, Han M, Song Z, Gao LH, Liu H, Zhong WJ, Yan JL (2017b) Zircon U–Pb geochronology and geochemistry of the post-collisional volcanic rocks in eastern Xinjiang Province, NW China: implications for the tectonic evolution of the Junggar terrane. Int Geol Rev:1–26

Eiler J (ed) (2003) Inside the subduction factory. Geophys Monogr Ser, vol 138. AGU, Washington, D.C., pp 311

Engebretson DC, Cox A, Gordon RG (1985) Relative motions between oceanic and continental plates in the Pacific basin. Geol Soc Am Spec Pap 206:1–60

Ernst WG, Tsujimori T, Zhang R, Liou JG (2007) Permo-Triassic collision, subduction-zone metamorphism, and tectonic exhumation along the east Asian continental margin. Annu Rev Earth Planet Sci 35:73–110

Fan WM, Guo F, Wang YJ, Lin G, Zhang M (2001) Post-orogenic bimodal volcanism along the Sulu orogenic belt in eastern China. Phys Chem Earth Solid Earth Geod 26(9–10):733–746

Foley SF, Jackson SE, Fryer BJ, Greenouch JD, Jenner GA (1996) Trace element partition coefficients for clinopyroxene and phlogopite in an alkaline lamprophyre from Newfoundland by LAM-ICP-MS. Geochim Cosmochim Acta 60:629–638

Furman T, Graham D (1999) Erosion of lithospheric mantle beneath the east African rift system: geochemical evidence from the Kivu volcanic province. Lithos 48:237–262

Gao S, Rudnick RL, Yuan HL, Liu XM, Liu YS, Xu WL, Ling WL, Ayers J, Wang XC, Wang QH (2004) Recycling lower continental crust in the North China craton. Nature 432(7019):892–897

Gencalioglu Kuscu G, Geneli F (2010) Review of post-collisional volcanism in the central Anatolian Volcanic Province (Turkey), with special reference to the Tepekoy volcanic complex. Int J Earth Sci 99: 593–621

Gerdes A, Wörner G, Henk A (2000) Post-collisional granite generation and HT–LP metamorphism by radiogenic heating: the Variscan South Bohemian Batholith. J Geol Soc 157:577–587

Gill JB (1981) Orogenic andesites and plate tectonics. Springer-Verlag, Heidelberg 390p

Gómez-Tuena A, Straub SM, Zellmer GF (2014) An introduction to orogenic andesites and crustal growth. Geol Soc Lond Spec Publ 385(1):1–13

Griffin WL, Wang X, Jackson SE, Pearson NJ, O'Reilly SY, Xu XS, Zhou XM (2002) Zircon chemistry and magma mixing, SE China: in-situ analysis of Hf isotopes, Tonglu and Pingtan igneous complexes. Lithos 61(3):237–269

Guo F, Fan W, Wang Y, Zhang M (2004) Origin of early cretaceous calc-alkaline lamprophyres from the Sulu orogen in eastern China: implications for enrichment processes beneath continental collisional belt. Lithos 78(3):291–305

Guo F, Fan W, Wang Y, Li C (2005) Petrogenesis and tectonic implications of early cretaceous high-K calc-alkaline volcanic rocks in the Laiyang Basin of the Sulu Belt, eastern China. Island Arc 14(2):69–90

Guo F, Fan W, Li CW, Wang CY, Li HX, Zhao L, Li JY (2014a) Hf–Nd–O isotopic evidence for melting of recycled sediments beneath the Sulu Orogen, North China. Chem Geol 381:243–258

Guo PY, Niu YL, Ye L, Liu JJ, Sun P, Cui HX, Zhang Y, Gao JP, Su L, Zhao JX, Feng YX (2014b) Lithosphere thinning beneath west North China craton: evidence from geochemical and Sr–Nd–Hf isotope compositions of Jining basalts. Lithos 202:37–54

Hacker BR, Ratschbacher L, Webb L, McWilliams MO, Ireland T, Calvert A, Dong SW, Wenk H, Chateigner D (2000) Exhumation of ultrahigh-pressure continental crust in east central China: late Triassic–early Jurassic tectonic unroofing. J Geophys Res Solid Earth 105(B6):13339–13364

Hacker BR, Wallis SR, Ratschbacher L, Grove M, Gehrels G (2006) High-temperature geochronology constraints on the tectonic history and architecture of the ultrahigh-pressure Dabie–Sulu Orogen. Tectonics 25(5)

Hawkesworth CJ, Hergt JM, Ellam RM, Mc Dermott F (1991) Element fluxes associated with subduction related magmatism. Phil Trans R Soc Lond A 335(1638):393–405

Hawthorne FC, Oberti R, Harlow GE, Maresch WV, Martin RF, Schumacher JC, Welch MD (2012) Nomenclature of the amphibole supergroup. Am Mineral 97(11–12):2031–2048

Heinrich KFJ, Romig Jr AD, Chambers WF (1986). Microbeam analysis. In: Romig AD Jr., Chambers WF (eds) Proc. 21st Int Conf, Albuquerque, NM pp. 279–80

Hermann J, Rubatto D (2014) Subduction of continental crust to mantle depth: geochemistry of ultrahigh-pressure rocks. Treat Geochem 4: 309–340

Hildreth W, Moorbath S (1988) Crustal contributions to arc magmatism in the Andes of central Chile. Contrib Mineral Petrol 98(4):455–489

Hofmann AW (1988) Chemical differentiation of the earth: the relationship between mantle, continental crust, and oceanic crust. Earth Planet Sci Lett 90:297–314

Hoskin PW, Ireland TR (2000) Rare earth element chemistry of zircon and its use as a provenance indicator. Geology 28:627–630

Hu ZC, Liu YS, Gao S, Liu WG, Zhang W, Tong XR, Lin L, Zong KQ, Li M, Chen HH, Zhou L, Yang L (2012) Improved in situ Hf isotope ratio analysis of zircon using newly designed X skimmer cone and jet sample cone in combination with the addition of nitrogen by laser ablation multiple collector ICP-MS. J Anal At Spectrom 27:1391–1399

Hu ZC, Zhang W, Liu YS, Gao S, Li M, Zong KQ, Chen HH, Hu SH (2015) "Wave" signal smoothing and mercury removing device for laser ablation quadrupole and multiple collector ICP-MS analysis: application to lead isotope analysis. Anal Chem 87:1152–1157

Ionov DA, Griffin WL, O'Reilly SY (1997) Volatile-bearing minerals and lithophile trace elements in the upper mantle. Chem Geol 141:153–184

Jahn BM, Wu F, Lo CH, Tsai CH (1999) Crust–mantle interaction induced by deep subduction of the continental crust: geochemical and Sr–Nd isotopic evidence from post-collisional mafic–ultramafic intrusions of the northern Dabie complex, central China. Chem Geol 157(1):119–146

Kelemen PB, Hanghoj K, Greene AR (2003a) One view of the geochemistry of subduction-related magmatic arcs, with an emphasis on primitive andesite and lower crust. Treat Geochem 3:593–659

Kelemen PB, Yogodzinski GM, Scholl DW (2003b) Along-strike variation in the Aleutian island arc: genesis of high mg# andesite and implications for continental crust. Inside the subduction factory. Geophys Monogr 138:223–276

Kuno H (1968) Origin of andesite and its bearing on the island arc structure. Bull Volcanol 32(1):141–176

Kusky TM, Windley BF, Wang L, Wang Z, Li X, Zhu P (2014) Flat slab subduction, trench suction, and craton destruction: comparison of the North China, Wyoming, and Brazilian cratons. Tectonophysics 630:208–221

Leake BE, Woolley AR, Arps CE, Birch WD, Gilbert MC, Grice JD et al (1997) Report. Nomenclature of amphiboles: report of the subcommittee on amphiboles of the international mineralogical association commission on new minerals and mineral names. Mineral Mag 61(2):295–321

Le Maitre RW (2002) Igneous rocks: a classification and glossary of terms. 2nd ed. Cambridge Univ Press, Cambridge, UK, pp 236

Li HY, Chen RX, Zheng YF, Hu ZC (2016) The crust–mantle interaction in continental subduction channels: zircon evidence from orogenic peridotite in the Sulu orogen. J Geophys Res Solid Earth 121:687–712

Li XP, Yan JY, Schertl HP, Kong FM, Xu H (2014) Eclogite from the Qianliyan Island in the Yellow Sea: a missing link between the mainland of China and the Korean peninsula. Eur J Mineral 26(6): 727–741

Liang YY, Deng J, Liu XF, Wang QF, Qin C, Li Y, Yang Y, Zhou M, Jiang JY (2018) Major and trace element, and Sr isotope compositions of clinopyroxene phenocrysts in mafic dykes on Jiaodong peninsula, southeastern North China craton: insights into magma mixing and source metasomatism. Lithos 302–303:480–495

Liati A, Gebauer D, Wysoczanski R (2002) U–Pb SHRIMP-dating of zircon domains from UHP garnet-rich mafic rocks and late pegmatoids in the Rhodope zone (N Greece); evidence for early cretaceous crystallization and late cretaceous metamorphism. Chem Geol 184(3):281–299

Liu FL, Liou JG (2011) Zircon as the best mineral for P–T–time history of UHP metamorphism: a review on mineral inclusions and U–Pb SHRIMP ages of zircons from the Dabie–Sulu UHP rocks. J Asian Earth Sci 40:1–39

Liu S, Zou HB, Hu RZ, Zhao JH, Feng GX (2006) Mesozoic mafic dikes from the Shandong peninsula, North China craton: petrogenesis and tectonic implications. Geochem J 40:181–195

Liu S, Hu R, Gao S, Feng C, Qi Y, Wang T, Feng GY, Coulson IM (2008) U–Pb zircon age, geochemical and Sr–Nd–Pb–Hf isotopic constraints on age and origin of alkaline intrusions and associated mafic dikes from Sulu orogenic belt, eastern China. Lithos 106(3):365–379

Liu S, Hu R, Gao S, Feng C, Yu B, Feng G, Qi YQ, Wang T, Coulson IM (2009) Petrogenesis of late Mesozoic mafic dykes in the Jiaodong peninsula, eastern North China craton and implications for the foundering of lower crust. Lithos 113(3):621–639

Liu S, Hu R, Gao S, Feng C, Feng G, Qi Y, Coulson IM, Yang YH, Yang CG, Tang L (2012) Geochemical and isotopic constraints on the age and origin of mafic dikes from eastern Shandong Province, eastern North China craton. Int Geol Rev 54(12):1389–1400

Liu YS, Hu ZC, Gao S, Günther D, Xu J, Gao CG, Chen HH (2008a) In situ analysis of major and trace elements of anhydrous minerals by LA-ICP-MS without applying an internal standard. Chem Geol 257: 34–43

Liu YS, Zong KQ, Kelemen PB, Gao S (2008b) Geochemistry and magmatic history of eclogites and ultramafic rocks from the Chinese continental scientific drill hole: subduction and ultrahigh-pressure metamorphism of lower crustal cumulates. Chem Geol 247:133–153

Ludwig K (2003) User's manual for Isoplot 3.00: a geochronological toolkit for Microsoft Excel. Berkeley Geochronology Center, Special Publications 1:1–55

Ma L, Jiang SY, Hofmann AW, Dai BZ, Hou ML, Zhao KD, Chen LH, Li JW, Jiang YH (2014a) Lithospheric and asthenospheric sources of lamprophyres in the Jiaodong peninsula: a consequence of rapid lithospheric thinning beneath the North China craton? Geochim Cosmochim Acta 124:250–271

Ma L, Jiang SY, Hou ML, Dai BZ, Jiang YH, Yang T, Zhao KD, Pu W, Zhu ZY, Xu B (2014b) Geochemistry of early cretaceous calc-alkaline lamprophyres in the Jiaodong peninsula: implication for lithospheric evolution of the eastern North China craton. Gondwana Res 25(2):859–872

Mao JW, Pirajno F, Cook N (2011) Mesozoic metallogeny in East China and corresponding geodynamic settings—an introduction to the special issue. Ore Geol Rev 43:1–7

McCulloch MT, Rosman KJ, De Laeter JR (1977) The isotopic and elemental abundance of ytterbium in meteorites and terrestrial samples. Geochim Cosmochim Acta 41:1703–1707

Morimoto N (1988) Nomenclature of pyroxenes. Mineral Petrol 39:55–76

Morrison GW (1980) Characteristics and tectonic setting of the shoshonite rock association. Lithos 13:97–108

Maruyama S, Isozaki Y, Kimura G, Terabayashi M (1997) Paleogeographic maps of the Japanese Islands: plate tectonic synthesis from 750 Ma to the present. Island Arc 6:121–142

Meng FX, Gao S, Song ZJ, Niu YL, Li XP (2018) Mesozoic high-Mg andesites from the Daohugou area, Inner Mongolia: upper-crustal fractional crystallization of parental melt derived from metasomatized lithospheric mantle wedge. Lithos 302–303:535–548

Ni J, Liu J, Tang X, Yang H, Xia Z, Guo Q (2013) The Wulian metamorphic core complex: a newly discovered metamorphic core complex along the Sulu orogenic belt, eastern China. J Earth Sci 24(3):297–313

Ni J, Liu J, Tang X, Yang H, Xia Z, Zhang T (2016) Early cretaceous exhumation of the Sulu orogenic belt as a consequence of the eastern Eurasian tectonic extension: insights from the newly discovered Wulian metamorphic core complex, eastern China. J Geol Soc 173(3):531–549

Nier AO (1938) The isotopic constitution of strontium, barium, bismuth, thallium and mercury. Phys Rev 54:275–278

Niu YL (2005) Generation and evolution of basaltic magmas: some basic concepts and a new view on the origin of Mesozoic–

Cenozoic basaltic volcanism in eastern China. Geol J China Univ 11(1):9–46

O'Nions RK, Hamilton PJ, Evensen NM (1977) Variations in $^{143}Nd/^{144}Nd$ and $^{87}Sr/^{86}Sr$ ratios in oceanic basalts. Earth Planet Sci Lett 34:13–22

Patiño Douce AE, Beard JS (1995) Dehydration-melting of biotite gneiss and quartz amphibolite from 3 to 15 kbar. J Petrol 36:707–738

Peacock SM (1993) Large-scale hydration of the lithosphere above subducting slabs. Chem Geol 108(1):49–59

Peccerillo A, Taylor SR (1976) Geochemistry of Eocene calc-alkaline volcanic rocks from the Kastamonu area, northern Turkey. Contrib Mineral Petrol 58:63–81

Pei FP, Xu WL, Yang DB, Yu Y, Wang W, Zhao QG (2011) Geochronology and geochemistry of Mesozoic mafic–ultramafic complexes in the southern Liaoning and southern Jilin provinces, NE China: constraints on the spatial extent of destruction of the North China craton. J Asian Earth Sci 40(2):636–650

Peng TP (2004) SHRIMP zircon U–Pb geochronology of the diorites for the southern Taihang Mountains in central north interior and its petrogenesis. Acta Petrol Sin 20:1253–1262 (In Chinese with English abstract)

Perfit MR, Gust DA, Bence AE, Arculus RJ, Taylor SR (1980) Chemical characteristics of island-arc basalts: implications for mantle sources. Chem Geol 30(3):227–256

Pidgeon RT (1992) Recrystallisation of oscillatory zoned zircon: some geochronological and petrological implications. Contrib Mineral Petrol 110(4):463–472

Qian Q, Hermann J (2013) Partial melting of lower crust at 10–15 kbar: constraints on adakite and TTG formation. Contrib Mineral Petrol 165:1195–1224

Rapp RP, Watson EB (1995) Dehydration melting of metabasalt at 8–32 kbar: implications for continental growth and crust–mantle recycling. J Petrol 36:891–931

Reubi O, Blundy J (2009) A dearth of intermediate melts at subduction zone volcanoes and the petrogenesis of arc andesites. Nature 461(7268):1269–1273

Rubatto D (2017) Zircon: the metamorphic mineral. Rev Mineral Geochem 83(1):261–295

Rumble D, Liou JG, Jahn BM (2003) Continental crust subduction and ultrahigh pressure metamorphism. Treat Geochem 3:293–319

Schaltegger U (1997) Magma pulses in the central Variscan Belt: episodic melt generation and emplacement during lithospheric thinning. Terra Nova 9(5–6):242–245

Seton M, Müller RD, Zahirovic S, Gaina C, Torsvik T, Shephard G, Talsma A, Gurnis M, Turner M, Maus S, Chandler M (2012) Global continental and ocean basin reconstructions since 200 Ma. Earth Sci Rev 113(3):212–270

Song ZG, Han ZZ, Gao LH, Geng HY, Li XP, Meng FX, Han M, Zhong WJ, Li JJ, Du QX, Yan JL, Liu H (2018) Permo-Triassic evolution of the southern margin of the central Asian Orogenic Belt revisited: insights from late Permian igneous suite in the Daheishan Horst, NE China. Gondwana Res 56:23–50

Spandler C, Pirard C (2013) Element recycling from subducting slabs to arc crust: a review. Lithos 170:208–223

Söderlund U, Patchett JP, Vervoort JD, Isachsen CE (2004) The ^{176}Lu decay constant determined by Lu−Hf and U−Pb isotope systematics of Precambrian mafic intrusions. Earth Planet Sci Lett 219:311–324

Stern CR, Kilian R (1996) Role of the subducted slab, mantle wedge and continental crust in the generation of adakites from the Andean Austral volcanic zone. Contrib Mineral Petrol 123:263–281

Stern RJ (2002) Subduction zones. Rev Geophys. https://doi.org/10.1029/2001RG000108

Straub SM, Gomez-Tuena A, Stuart FM, Zellmer GF, Espinasa-Perena R, Cai Y, Iizuka Y (2011) Formation of hybrid arc andesites beneath thick continental crust. Earth Planet Sci Lett 303(3):337–347

Sun SS, McDonough WF (1989) Chemical and isotopic systematics of oceanic basalts: implications for mantle composition and processes. Geol Soc Lond Spec Publ 42:313–345

Tang J, Zheng YF, Wu YB, Gong B, Zha X, Liu X (2008) Zircon U–Pb age and geochemical constraints on the tectonic affinity of the Jiaodong terrane in the Sulu orogen, China. Precambrian Res 161(3):389–418

Tang HY, Zheng JP, Yu CM (2009) Age and composition of the Rushan intrusive complex in the northern Sulu orogeny, eastern China: petrogenesis and lithospheric mantle evolution. Geol Mag 146(2):199–215

Taylor SR, McLennan SM (1995) The geochemical evolution of the continental crust. Rev Geophys 33(2):241–265

Van der Meer DG, Torsvik TH, Spakman W, van Hinsbergen DJJ, Amaru ML (2012) Intra-Panthalassa Ocean subduction zones revealed by fossil arcs and mantle structure. Nat Geosci 5:215–219

Vervoort JD, Blichert-Toft J (1999) Evolution of the deleted mantle: Hf isotope evidence from juvenile rocks through time. Geochim Cosmochim Acta 63:533–556

Wang L, Kusky TM, Polat A, Wang SJ, Jiang X, Zong K, Wang JP, Deng H, Fu J (2014) Partial melting of deeply subducted eclogite from the Sulu orogen in China. Nat Commun 5:5604

Wang L, Wang SJ, Brown M, Zhang JF, Feng P, Jin ZM (2018) On the survival of intergranular coesite in UHP eclogite. J Metamorph Geol 36:173–194

Wang LG, Qiu YM, McNaughton NJ, Groves DI, Luo ZK, Huang JZ, Miao LC, Liu YK (1998) Constraints on crustal evolution and gold metallogeny in the northwestern Jiaodong peninsula, China, from SHRIMP U–Pb zircon studies of granitoids. Ore Geol Rev 13(1–5):275−−291

Wang SJ, Wang L, Brown M, Feng P (2016) Multi-stage barite crystallization in partially melted UHP eclogite from the Sulu belt, China. Am Mineral 101:564–579

Wang SJ, Wang L, Brown M, Piccoli PM, Johnson TE, Feng P, Deng H, Kitajima K, Huang Y (2017) Fluid generation and evolution during exhumation of deeply subducted UHP continental crust: petrogenesis of composite granite–quartz veins in the Sulu belt, China. J Metamorph Geol 35(6):601–629

Whitney DL, Evans BW (2010) Abbreviations for names of rock-forming minerals. Am Mineral 95:185–187

Wiedenbeck M, Allé P, Corfu F, Griffin WL, Meier M, Oberli F, Quadt A, Roddick JC, Spiegel W (1995) Three natural zircon standards for U−Th−Pb, Lu−Hf, trace element and REE analyses. Geostand Newslett 19(1):1–23

Winchester JA, Floyd PA (1977) Geochemical discrimination of different magma series and their differentiation products using immobile elements. Chem Geol 20:325–343

Wu FY, Lin JQ, Wilde SA, Zhang XO, Yang JH (2005) Nature and significance of the early cretaceous giant igneous event in eastern China. Earth Planet Sci Lett 233(1):103–119

Xia B, Brown M, Wang L, Wang SJ, Piccoli P (2018) Phase equilibrium modeling of MT–UHP eclogite: a case study of coesite eclogite at Yangkou Bay, Sulu belt. Eastern China J Petrol. https://doi.org/10.1093/petrology/egy060

Xu JW, Zhu G (1994) Tectonic models of the tan-Lu fault zone, eastern China. Int Geol Rev 36(8):771–784

Xu YG, Huang XL, Ma JL, Wang YB, Iizuka Y, Xu JF, Wang Q, Wu XY (2004a) Crust–mantle interaction during the tectono-thermal reactivation of the North China craton: constraints from SHRIMP zircon U–Pb chronology and geochemistry of Mesozoic plutons from western Shandong. Contrib Mineral Petrol 147(6):750–767

Xu YG, Ma JL, Huang XL, Iizuka Y, Chung SL, Wang YB, Wu XY (2004b) Early cretaceous gabbroic complex from Yinan, Shandong province: petrogenesis and mantle domains beneath the North China craton. Int J Earth Sci 93:1025–1041

Yang CH, Xu W, Yang D, Wang W, Wang W, Liu J (2008) Petrogenesis of Shangyu gabbro-diorites in western Shandong: geochronological and geochemical evidence. Sci China Ser D Earth Sci 51(4):481–492

Yang DB, Xu WL, Pei FP, Yang CH, Wang QH (2012) Spatial extent of the influence of the deeply subducted South China block on the southeastern North China block: constraints from Sr–Nd–Pb isotopes in Mesozoic mafic igneous rocks. Lithos 136–139:246–260

Yang JH, Wu FY, Wilde SA (2003) A review of the geodynamic setting of large-scale late Mesozoic gold mineralization in the North China craton: an association with lithospheric thinning. Ore Geol Rev 23: 125–152

Yang JH, Wu FY, Chung SL, Wilde SA, Chu MF, Lo CH, Song B (2005) Petrogenesis of early cretaceous intrusions in the Sulu ultrahigh-pressure orogenic belt, East China and their relationship to lithospheric thinning. Chem Geol 222(3):200–231

Yang W, Li SG (2008) Geochronology and geochemistry of the Mesozoic volcanic rocks in Western Liaoning: implications for lithospheric thinning of the North China craton. Lithos 102:88–107

Yoshida D, Hirajima T, Ishiwatari A (2004) Pressure–temperature path recorded in the Yangkou garnet peridotite, in Su-Lu ultrahigh-pressure metamorphic belt, eastern China. J Petrol 45(6):1125–1145

Zhang HF, Sun M, Zhou XH, Fan WM, Zhai MG, Yin JF (2002) Mesozoic lithosphere destruction beneath the North China craton: evidence from major-, trace-element and Sr–Nd–Pb isotope studies of Fangcheng basalts. Contrib Mineral Petrol 144:241–253

Zhang J, Zhao ZF, Zheng YF, Liu X, Xie L (2012) Zircon Hf–O isotope and whole-rock geochemical constraints on origin of postcollisional mafic to felsic dykes in the Sulu orogen. Lithos 136:225–245

Zhang SH, Zhao Y, Davis GA, Ye H, Wu F (2014) Temporal and spatial variations of Mesozoic magmatism and deformation in the North China craton: implications for lithospheric thinning and decratonization. Earth Sci Rev 131:49–87

Zhao D, Ohtani E (2009) Deep slab subduction and dehydration and their geodynamic consequences: evidence from seismology and mineral physics. Gondwana Res 16(3):401–413

Zhao ZF, Dai LQ, Zheng YF (2013) Postcollisional mafic igneous rocks record crust-mantle interaction during continental deep subduction. Sci Rep 3:3413

Zhao ZF, Zheng YF, Chen RX, Xia QX, Wu YB (2007) Element mobility in mafic and felsic ultrahigh-pressure metamorphic rocks during continental collision. Geochim Cosmochim Acta 71(21):5244–5266

Zhao ZF, Zheng YF, Zhang J, Dai LQ, Li Q, Liu X (2012) Syn-exhumation magmatism during continental collision: evidence from alkaline intrusives of Triassic age in the Sulu orogen. Chem Geol 328:70–88

Zheng YF (2012) Metamorphic chemical geodynamics in continental subduction zones. Chem Geol 328:5–48

Zheng YF, Wu YB, Zhao ZF, Zhang SB, Xu P, Wu FY (2005) Metamorphic effect on zircon Lu–Hf and U–Pb isotope systems in ultrahigh-pressure eclogite-facies metagranite and metabasite. Earth Planet Sci Lett 240:378–400

Zheng YF, Xu Z, Zhao ZF, Dai LQ (2018) Mesozoic mafic magmatism in North China: implications for thining and destruction of cratonic lithosphere. Sci China: Earth Sci 61(4):353–383

Zong KQ, Klemd R, Yuan Y, He ZY, Guo JL, Shi XL, Liu YS, Hu ZC, Zhang ZM (2017) The assembly of Rodinia: the correlation of early Neoproterozoic (ca. 900 Ma) high-grade metamorphism and continental arc formation in the southern Beishan Orogen, southern central Asian Orogenic Belt (CAOB). Precambrian Res 290:32–48